

Genesis of Chating Cu-Au deposit in the Middle-Lower Yangtze River Metallogenic Belt, Eastern China: Implications from magnetite and biotite geochemistry



Qing-Ling Xiao^{a,b}, Tao-Fa Zhou^{a,b,*}, Shi-Wei Wang^{a,b}, Feng Yuan^{a,b}, Noel C. White^{a,b,c}, Fang-Yue Wang^{a,b}, Zu-Jun Xie^d, Jing Liu^{a,d}

^a School of Resources and Environmental Engineering, Hefei University of Technology, Hefei 230009, China

^b Ore Deposit and Exploration Centre (ODEC), Hefei University of Technology, Hefei 230009, China

^c Centre of Excellence in Ore Deposit (CODES), University of Tasmania, Private Bag 79, Hobart, Australia

^d No.322 Unit of Bureau of Geology and Mineral Exploration of Anhui Province, Ma'anshan, Anhui 246000, China

ARTICLE INFO

Keywords:

Biotite
Magnetite
Chatong deposit
Xuancheng district
MLYB

ABSTRACT

Porphyry deposits developed in intracontinental settings have some geological characteristics that differ from those developed in arc-related continental margins. The Chatong deposit is a newly discovered Cu-Au deposit in the Middle-Lower Yangtze River Metallogenic Belt (MLYB), eastern China. We carried out detailed petrographic observations and major and trace element analyses of different types of magnetite and biotite from the host quartz diorite porphyry and different alteration zones in Chatong to elucidate the genesis of Chatong deposit.

Alteration types in Chatong include skarn, sodic-calcic, potassic and phyllitic, and copper mineralization is closely associated with potassic alteration of quartz diorite porphyry. The different types of magnetite and biotite at Chatong show distinctive geochemical characteristics. Higher Ti and Al in magmatic magnetites and biotites compared to the hydrothermal minerals indicate higher temperature and pressure in the quartz diorite porphyry. Higher V in magmatic magnetites and lower X_{Mg} in magmatic biotites indicate higher fO_2 . Similar mineral geochemistry from typical worldwide porphyry deposits, for example, Al_2O_3 , TiO_2 , FeO^T , MgO , Na_2O , IV(F) and IV(Cl) contents in biotite, and Ni/Cr, Ti, Al, Sn and Ga in magnetite, indicate a predominately magmatic fluid source. Differences in Si, Ca, Co/Ni, Mg, and Mn in different types of magnetite, and MnO , CaO , SiO_2 differences in two types of biotite from typical porphyry copper deposits show the influence of external fluids. Moreover, high IV(F) values and low IV(Cl) values in biotites demonstrate that the magmatic-hydrothermal system in Chatong was enriched in Cl and lacked F, consistent with the importance of Cl in the transport of Cu. Based on different discrimination diagrams for magnetite, such as Ni/Cr versus Ti, Ni/(Cr + Mn) versus Ti + V, and Al + Mn versus Ti + V, and the geochemical similarities of biotite from Chatong and other porphyry deposits, combined with the similarity of alteration assemblages, we conclude that Chatong has porphyry Cu-Au affinities, but the hydrothermal system was affected by external fluids, in contrast to more typical subduction-related porphyry deposits.

1. Introduction

The Middle-Lower Yangtze River Metallogenic Belt (MLYB), located in the central-eastern region of China, is characterized by porphyry-skarn copper-gold deposits and magnetite-apatite iron deposits that formed in an intracontinental setting (Chang et al., 1991; Pirajno and Zhou, 2015; Zhou et al., 2012, 2015, 2016; Fig. 1). Representative deposits include Jiguanzui porphyry Cu-Au deposit in the Edong ore district (Zhang, 2015), Shaxi porphyry Cu-Au deposit in the Luzong ore

district (Wang et al., 2014, 2015), Shuijadian porphyry Cu deposit in the Tongling ore district (Wang et al., 2012), and Washan iron deposit in the Ningwu ore district (Duan et al., 2012). Compared to typical porphyry deposits developed in magmatic arc settings, porphyry deposits in the MLYB have different geological characteristics (Zhou et al., 2015). What caused these differences is still ambiguous, and more investigations of the porphyry-skarn Cu-Au deposits from the MLYB need to be done in order to understand the mechanism.

Xuancheng is a newly discovered ore district in the MLYB, and

* Corresponding author at: School of Resources and Environmental Engineering, Hefei University of Technology, Hefei 230009, China.
E-mail address: tfzhou@hfut.edu.cn (T.-F. Zhou).

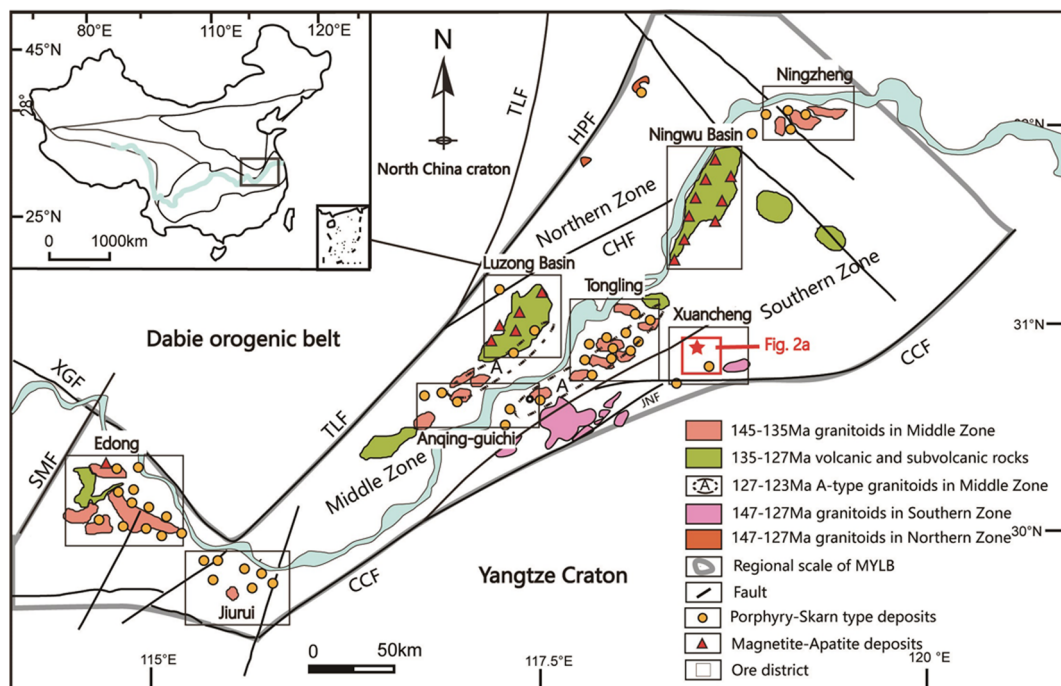


Fig. 1. Geological sketch map of Middle-Lower Yangtze River Metallogenic Belt (modified after Chang et al., 1991; Mao et al., 2011; Zhou et al., 2017). XGF: Xiangfan-Guangji Fault, TLF: Tanlu Fault, HPF: Huanglishu-Poliangting Fault, CHF: Chuhe Fault, SMF: Shangma-Tuanfeng-Liangzhi Fault, CCF: Chongyang-Changzhou Fault, JNF: Jiangnan Fault.

numerous copper and iron deposits have been found, e.g., Chating Cu-Au deposit, Magushan Cu-Mo deposit and Shizishan Cu deposit (Fig. 2a; Bian, 1995; Hong et al., 2017; Huang et al., 2013; Jiang, 2017; Qian et al., 2017). Chating is the biggest Cu-Au deposit in Xuancheng district (> 0.5 Mt Cu at 0.58% and > 65 t Au at 0.71 g/t), but its geological characteristics and genesis have not been previously investigated.

Most porphyry-skarn deposits in the MLYB have been studied in terms of geochronology, fluid inclusion characteristics and stable isotopes. With the development of *in situ* element analysis techniques, for example, laser ablation inductively coupled plasma mass spectrometry (LA-ICP-MS) and electron microprobe (EMPA), mineral chemistry has also become a useful method in determining the physicochemical conditions of magmatic and hydrothermal processes in porphyry-skarn deposits. Magnetite and biotite are common in magmatic rocks and hydrothermal alteration zones, and the controlling factors of their mineral chemistry have been well studied (Czamanske et al., 1973; Dupuis and Beaudoin, 2011; Munoz, 1984; Mollo et al., 2013; Nadoll et al., 2014a,b, 2015; Speer, 1987; Wones et al., 1965).

Magnetite is a common and widespread mineral in magmatic, sedimentary and metamorphic rocks, and can also precipitate in different kinds of hydrothermal deposits including skarn, IOCG, and porphyry deposits (Dupuis and Beaudoin, 2011; Nadoll et al., 2010, 2011, 2012, 2014a,b, 2015). As a member of the spinel group, the Fe^{2+} and Fe^{3+} in magnetite can be replaced by other cations. Divalent cations such as Mg, Ni, Mn, Co, or Zn commonly occupy the site of Fe^{2+} , whereas trivalent cations such as Al, Cr, V, Ga enter the site of Fe^{3+} (Lindsley, 1976; Wechsler et al., 1984; Wood et al., 1991). Other cations such as Ti^{4+} can occupy the Fe^{3+} by coupled substitution. The mineral chemistry of magnetite is also controlled by: (1) composition of precipitating fluids, (2) temperature, (3) oxygen or sulfur fugacity, (4) fluid-host rock interactions, and (5) co-crystallizing minerals

(Buddington and Lindsley, 1964; Dare et al., 2014; Frost and Lindsley, 1991; Nadoll et al., 2014a,b; Toplis and Carroll, 1995).

Biotite, $(\text{K}, \text{Na}, \text{Ca}, \text{Ba}) (\text{Fe}^{2+}, \text{Fe}^{3+}, \text{Mg}, \text{Ti}, \text{Mn}, \text{Al})_8 (\text{Si}, \text{Al})_4 \text{O}_{10} (\text{OH}, \text{F}, \text{Cl})_2$, is a widespread hydrous mineral in felsic intrusions, and it can also be found in hydrothermal alteration systems (Jacobs et al., 1976, 1979). Biotite mineral chemistry can be used to indicate the temperature, pressure, composition and redox conditions of magmatic and hydrothermal systems (Czamanske et al., 1973; Munoz, 1984; Speer, 1987; Wones et al., 1965). Especially in porphyry ore deposit systems, biotite is a common mineral in porphyritic intrusive rocks and in hydrothermal alteration zones, and can provide information on conditions in the study of the magmatic and hydrothermal processes.

Many studies about magnetite and biotite geochemistry have been published in recent years to infer deposit genesis and to determine the physicochemical conditions during hydrothermal evolution. Examples include using magnetite geochemistry to discuss the genesis of different iron deposits such as Chenchao, Washan, Tieshan and Fenghuangshan in the MLYB (Hu et al., 2014; Li et al., 2016; Duan et al., 2012); using magmatic and hydrothermal magnetite compositions to locate or explore porphyry deposits (Nadoll et al., 2015; Canil et al., 2016; Pisak et al., 2017); and using magmatic and hydrothermal biotite to determine the physicochemical conditions and elucidate the magmatic-hydrothermal fluid evolution in porphyry systems (Boomeri et al., 2009; Ayati et al., 2008; Afshooni et al. (2013); Tang et al., 2017; Jin et al., 2018).

In this study, we present new petrographic descriptions and *in situ* major and trace element data for magmatic and hydrothermal magnetite and biotite, using EMPA and LA-ICP-MS techniques to characterize and constrain the genesis of Chating deposit.

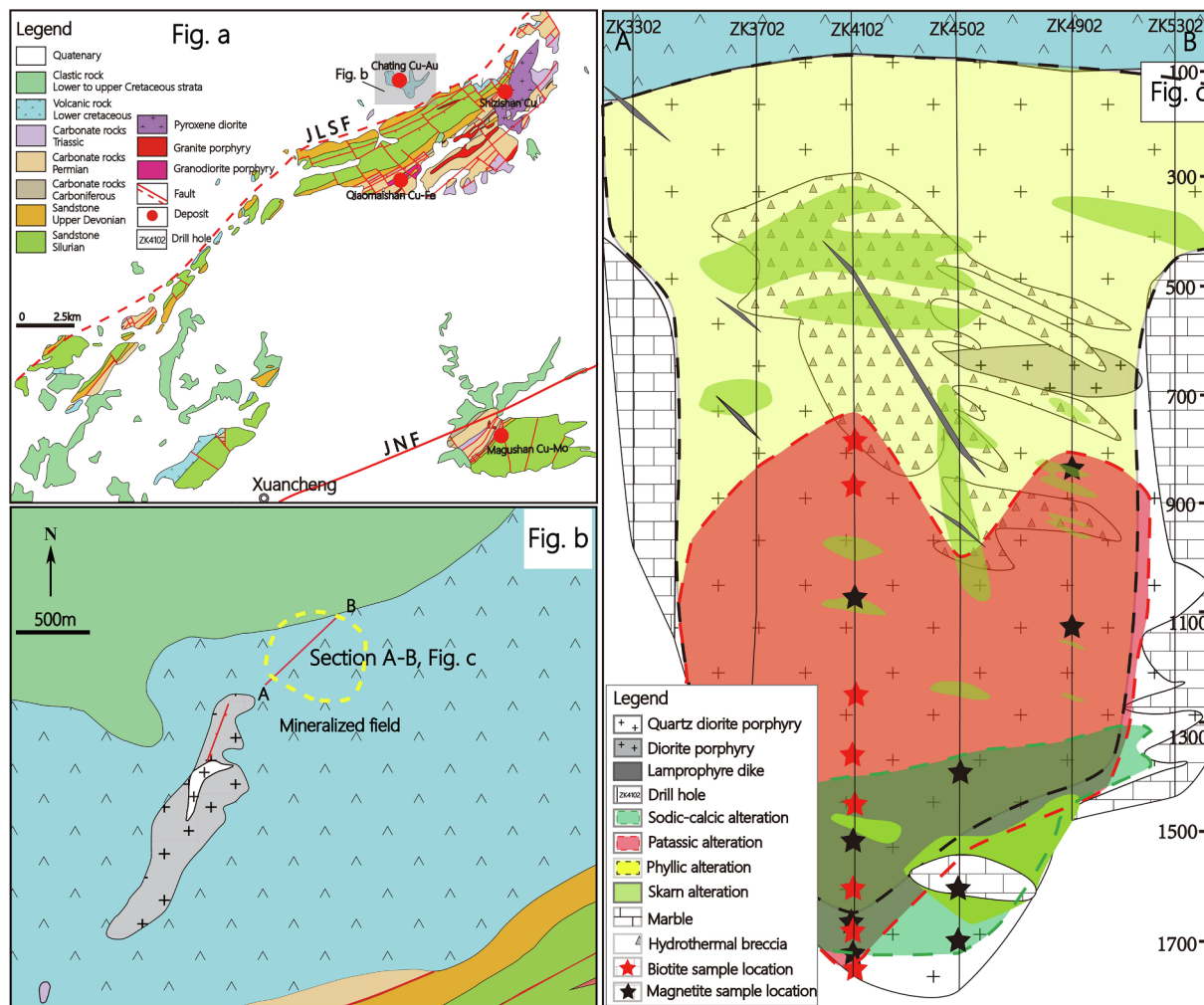


Fig. 2. (a) Geological sketch map of the Xuancheng ore district; (b) Basement geological map of Chating Cu-Au deposit (modified after No.322 Unit of Bureau of Geology and Mineral Exploration of Anhui Province); (c) Section A-B of Chating Cu-Au deposit with sampling locations.

2. Geological background

2.1. Regional geology

The MLYB is located in the north-eastern margin of the Yangtze Craton and along the southeastern margin of the North China Craton and the Dabie Orogenic Belt. It is bounded by the Xiangfan-Guangji Fault (XGF) to the northwest, the Huanglishu-Poliangting Fault (HPF) to the northeast and the Chongyang-Changzhou Fault (CCF) to the south (Fig. 1). The MLYB can be subdivided into three subzones, the southern, middle and northern subzone (Zhou et al., 2017). The northern subzone is characterized by copper, gold and a few lead and zinc deposits located along the HPF. The southern subzone is characterized by copper, molybdenum, gold, tungsten and antimony deposits. The middle subzone is the main ore-hosting zone in the MLYB and contains seven ore deposit districts; Edong, Jiurui, Anqing, Luzong, Tongling, Ningwu and Ningzhen from west to east. Xuancheng is located between the southern and middle subzones, and is a new ore district characterized by copper, molybdenum and gold deposits (Fig. 1; Chang et al., 1991; Zhou et al., 2012, 2015, 2016, 2017).

Most of the Xuancheng ore district is covered by Quaternary sediments and volcanic rocks of the Cretaceous Zhongfencun Formation and clastic rocks of the Xuannan Formation (Fig. 2a), Triassic carbonate

rocks mainly occur at the northeastern part of Xuancheng area. Two NE-trending faults named the Jiulianshan thrust fault (JLSF) and the Jiangnan fault (JNF), a series of NW faults and a NE-trending fold controlled the distribution of magmatic rocks in this area. The intrusive rocks are dominantly granite porphyry, granodiorite porphyry, quartz diorite porphyry and pyroxene diorite (Fig. 2a).

2.2. Deposit Geology

Chating is a concealed deposit, located in the northeast of the Xuancheng ore district and north of the Jiulianshan thrust fault (Fig. 2a). The wall rocks of Chating are carbonates from Triassic Nanninghu Formation which are now marble. Diorite porphyry and quartz diorite porphyry to the southwest of Chating may be connected to the mineralized intrusions at depth (Fig. 2b). The mineralized quartz diorite porphyry and diorite porphyry are the main intrusive rocks; they are cut by late lamprophyre dikes (Fig. 2c). Geochronology shows the quartz diorite porphyry and diorite porphyry have similar ages of 135.9–137.8 Ma (Jiang, 2017). No copper or gold mineralization is known in the diorite porphyry, but phyllitic alteration is widespread. All the wall rocks and magmatic rocks in Chating are strongly altered. Alteration types are mainly skarn, potassic, sodic-calcic, and phyllitic assemblages (Fig. 2c). In contrast to typical porphyry deposits in

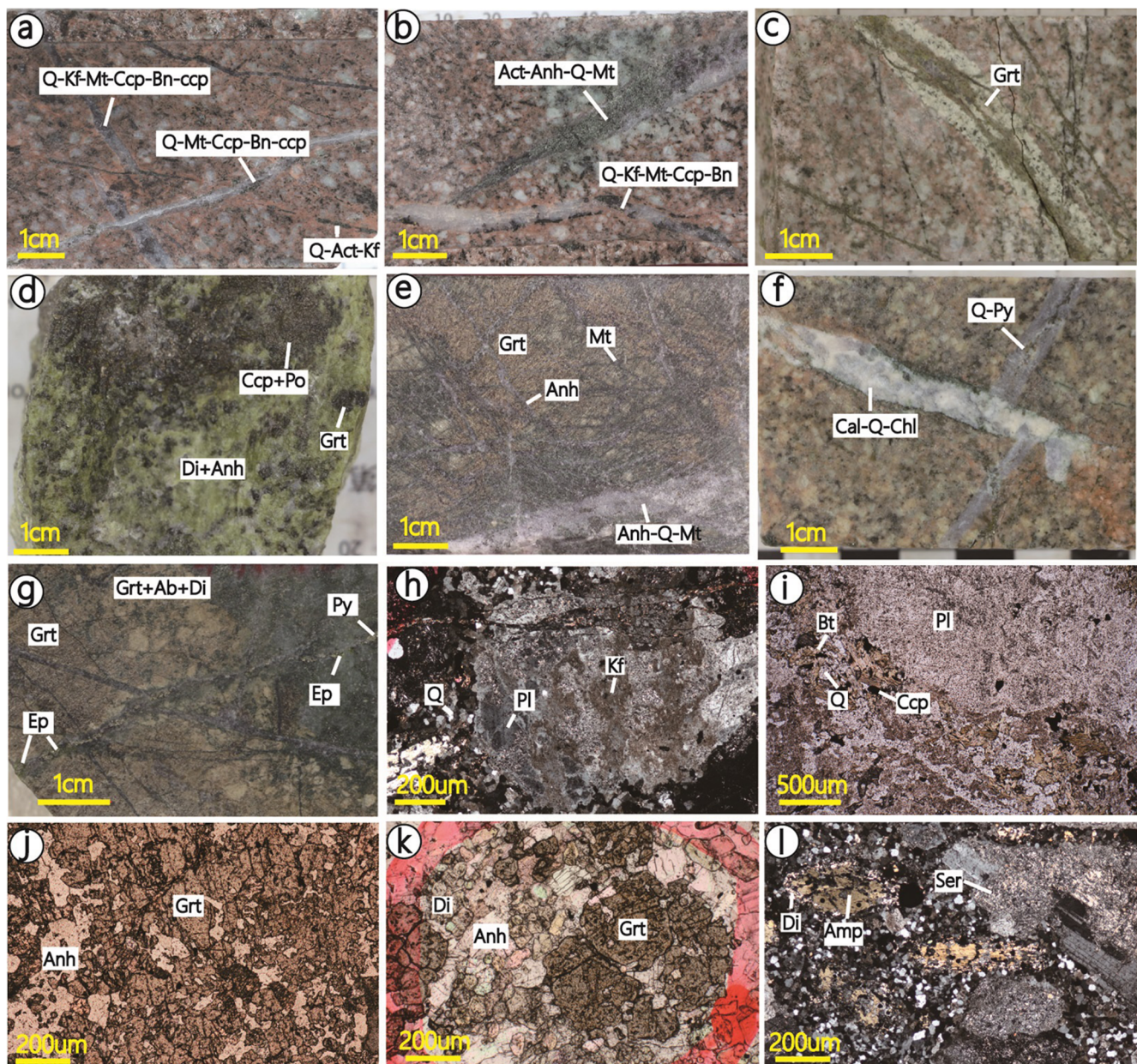


Fig. 3. Photographs of samples from different alteration zones. a. Crosscutting Q-Mt-Ccp-Bn ± Kf veins from potassic alteration; b. Q-Mt-Ccp-Bn-Kf cutting an Anh-Act-Q-Mt vein; c. Fine-grained garnet vein from sodic-calcic alteration; d. Exoskarn with assemblages of Anh, Mt, Di, Grt, Po and Ccp; e. Endoskarn with assemblages of Grt, Di, Anh and Mt; f. Cal-Q-Chl vein cutting a Q-Py vein in phyllitic alteration; g. Py-Ep vein cutting a Q-Anh vein and endoskarn; h. Kf replacing Pl phenocrysts; i. Bt-Ccp vein in potassic alteration zone; j. Endoskarn composed of coarse Grt and Anh; k. Exoskarn composed of Grt, Anh and Di; l. Di replacing Amp, and Ser replacing Pl. Act: actinolite, Anh: anhydrite, Bn: bornite, Cal: calcite, Ccp: chalcopyrite, Chl: chlorite, Di: diopside, Ep: epidote, Grt: garnet, Kf: K-feldspar, Mt: magnetite, Pl: plagioclase, Po: pyrrhotite; Q: quartz; Ser: sericite.

magmatic arc settings, propylitic alteration in Chating is very weakly developed, due to the carbonate host rocks. Minor epidote-pyrite veins occur at depths of 1822 m and 1206 m (Fig. 3g).

Copper and gold mineralization is hosted in quartz ± anhydrite ± magnetite-sulfides veins in quartz diorite porphyry. A distinctive feature of Chating deposit is a large hydrothermal breccia body that occurs above the main ore zone (Fig. 2c). We present detailed descriptions of the alteration, mineralization and breccia below.

2.2.1. Skarn alteration

Skarn alteration in the quartz diorite porphyry occurs at all levels from deep to shallow. It can be divided into endoskarn and exoskarn. Endoskarn occurs along planar zones in quartz diorite porphyry; it is mainly composed of massive garnet and diopside replacing plagioclase and amphibole, accompanied by some disseminated magnetite and chalcopyrite (Fig. 3e, g). Exoskarn occurs on the contact between quartz diorite porphyry and carbonate rocks in deep drill holes 4502 and 4902 (Fig. 2c), and it is mainly composed of garnet, diopside, anhydrite, and

calcite (Fig. 3d, k), with minor disseminated magnetite.

2.2.2. Sodic-calcic alteration

Sodic-calcic alteration developed in the deep part of the quartz diorite porphyry below 1300 m. It mainly appears in veins, including garnet veins, anhydrite-actinolite-diopside-magnetite veins, and anhydrite-diopside veins with garnet and albite halos (Fig. 3c). They are all cut by quartz-K-feldspar-magnetite-chalcopyrite-bornite veins (Fig. 3b) associated with potassic alteration. On the margins of the different kind of veins, Na- and Ca-rich minerals such as diopside replace amphiboles, and albite replaces plagioclase; the same assemblage also occurs dispersed in the sodic-calcic alteration zone (Fig. 3l). Few sulfide minerals occur in the sodic-calcic alteration.

2.2.3. Potassic alteration

Potassic alteration is widespread in Chating and it hosts most of the ore minerals. It is spatially associated with the quartz diorite porphyry and occurs below about 950 m; it is overlapped by phyllitic alteration. The minerals in the potassic alteration zone are mainly K-feldspar and biotite, as well as some accessory minerals such as anhydrite, magnetite, chalcopyrite and bornite (Fig. 3a, b, h and i). The plagioclase in the groundmass and partly in phenocrysts is altered to K-feldspar, resulting in the red color of the quartz diorite porphyry. Amphiboles are partly replaced by flakes of hydrothermal biotite (Fig. 6c). Veins in the potassic alteration occur as biotite veinlets and quartz-chalcopyrite-bornite-magnetite veins with K-feldspar halos (Fig. 3b).

2.2.4. Phyllitic alteration

Phyllitic alteration is the most widespread alteration, and overprints

the earlier potassic and sodic-calcic alteration. The phyllitic assemblage minerals are quartz, chlorite, calcite and sericite that replaced primary magmatic minerals and earlier hydrothermal minerals (Fig. 3f, l).

2.2.5. Breccia

Hydrothermal breccias mostly occur at depths between 400 m and 1000 m. Clasts in the breccia are mainly of quartz diorite porphyry, many showing quartz-pyrite veins truncated at their margins; clasts of skarn, vein quartz and anhydrite vein fragments also occur. The breccia cement is dominantly quartz, anhydrite, and pyrite with minor chalcopyrite. The entire breccia body is overlapped by phyllitic alteration; it does not contain magnetite or biotite.

2.2.6. Mineral paragenesis

Based on the mineral assemblages and vein crosscutting relationships, we subdivided the alteration and mineralization into three stages: stage I, pre-ore stage, including sodic-calcic and skarn alteration; stage II, ore-forming stage, including potassic and phyllitic alteration; stage III, post-ore stage, mainly calcite alteration. Because the timing relationship between sodic-calcic and skarn alteration is ambiguous, and both are cut by potassic alteration veins, we allocated them to the pre-ore stage. Ore mineralization is closely related to potassic alteration. Fig. 4 summarizes the paragenetic sequence of minerals in Chating deposit.

3. Mineral petrography

We separated magnetite and biotite into several types based on the petrographic characteristics of samples. Detailed descriptions of representative samples are presented in Table 1.

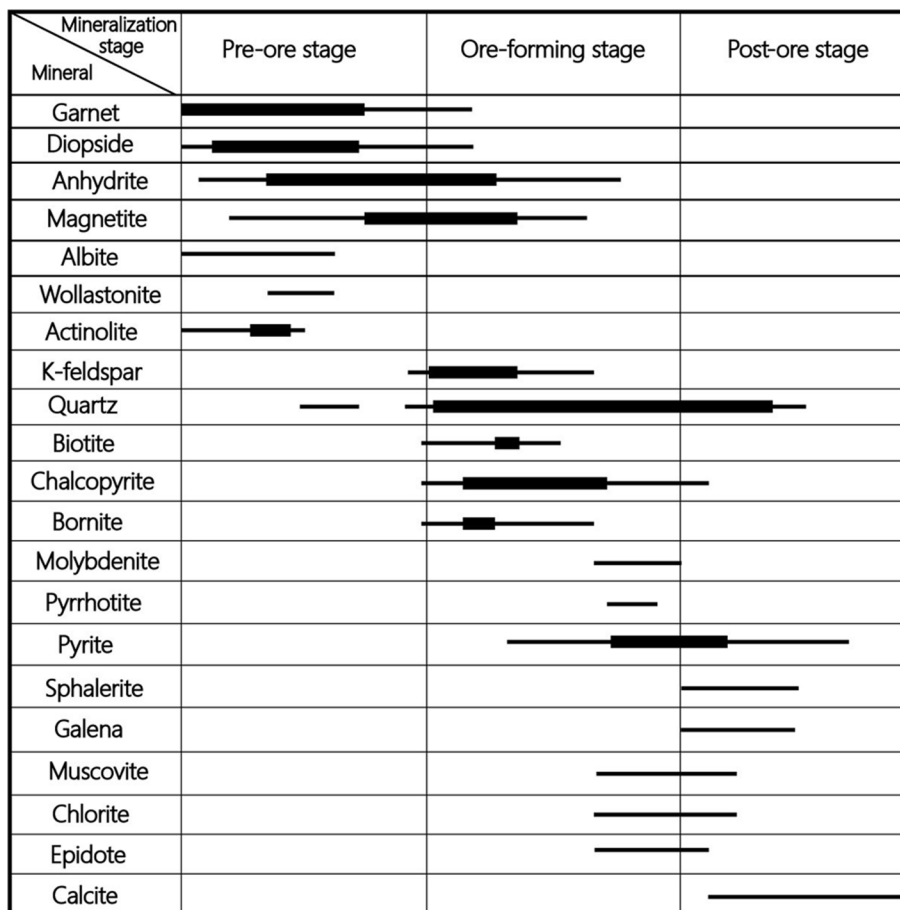


Fig. 4. Mineralization paragenesis of the Chating Cu-Au deposit.

Table 1

Detailed description of analyzed magnetite and biotite samples.

Type	Sample	Texture	Coexisting mineral assemblage
Mt from quartz diorite porphyry	M-910	< 200 µm grains in the matrix of quartz diorite porphyry, euhedral to subhedral	Surrounded by fine-grained quartz, K-feldspar and plagioclase
	M-1537	> 300 µm, disseminated grains in endoskarn, subhedral to anhedral	Sulfides such as Ccp and Bn, silicate minerals such as Di, Anh and Grt
Mt from exoskarn zone	M-1025	> 300 µm, disseminated grains in endoskarn, subhedral to anhedral	Small amount of Ccp, and silicate minerals such as Di, Anh and Grt
	M-1002	< 150 µm, sparsely disseminated and fine-grained in exoskarn, subhedral	Accompanied with a little fine-grained Bn, and Act, Anh and Ab
Mt from sodic-calcic alteration zone	M-1614	< 150 µm, sparsely disseminated and fine-grained in exoskarn, subhedral	Accompanied with a little fine-grained Bn, and Act, Anh and Ab
	M-1561	220–550 µm grains in 1–5 mm veins, euhedral to subhedral	Accompanied with Bn, Ccp and Py, and Q, Anh and Kf
Mt from potassic alteration zone	M-1722	< 300 µm grains in 0.5–3 mm veins, subhedral to anhedral	Accompanied with Bn, Ccp and Py, and Q, Anh and Kf
	M-10		
Magmatic biotite from quartz diorite porphyry	M-1695		
	B-868	0.3–1 mm phenocrystal in quartz diorite porphyry, euhedral	Coexisting with fine-grained euhedral apatite, partly replaced by chlorite
Hydrothermal biotite from potassic alteration zone	B-910		
	B-1242		
	B-1400		
	B-1722		
	B-10		
	B-1756	0.3–2 mm grains in biotite veins or aggregates of fine-grained flakes replaced amphiboles	Accompanied with Mt, Bn, Ccp and Py
	B-910		
	B-868		
	B-1		
	B-1400		

3.1. Magnetite petrography

Magnetite is widespread in the quartz diorite porphyry and in different alteration zones. It can be divided into two broad types: magmatic magnetite from the least-altered parts of intrusions, and hydrothermal from veins. Based on different alteration, we subdivide the hydrothermal magnetite into four groups: magnetite from sodic-calcic, potassic, exoskarn and endoskarn alteration.

Magmatic magnetite is sparsely distributed in the quartz diorite porphyry; crystals are euhedral to subhedral, 100–200 µm in diameter (Fig. 5h). Magnetite from sodic-calcic alteration occurs in anhydrite-actinolite-diopside-magnetite veins (Fig. 5g) where it is accompanied by minor bornite; the magnetite grains are euhedral to subhedral, and 200–550 µm across. Magnetite from potassic alteration occurs in quartz-K-feldspar-magnetite-chalcopyrite-bornite veins or disseminated in quartz diorite porphyry as anhedral crystals (Fig. 5e, f). Magnetite from skarn alteration can be subdivided into exoskarn and endoskarn magnetite. Exoskarn magnetites are always sparsely disseminated and fine-grained (Fig. 5a, b), 50–150 µm across. Endoskarn magnetites occur in the quartz diorite porphyry (Fig. 5c, d), and are larger than exoskarn magnetites.

3.2. Biotite petrography

Biotites in Chating deposit can be divided into magmatic and hydrothermal types. Magmatic biotites occur as isolated crystals with euhedral to subhedral crystal shapes in the quartz diorite porphyry; they vary from 500 to 1500 µm in size (Fig. 6a, b). Hydrothermal biotites mainly occur as veinlets, or aggregates of fine-grained flakes accompanied by some chalcopyrite and bornite, or replacing amphiboles or magmatic biotites in the potassic alteration zone (Fig. 6c, d).

4. Methods

After careful observation of the minerals under an optical microscope, a JEOL JXA-8230 EMPA was used to obtain the major composition of the different types of biotite. The EMPA analysis was

accomplished in the EMPA laboratory at the School of Resource and Environmental Engineering in Hefei University of Technology, using a voltage of 15 kV and a beam current of 20 nA focused to a spot of 3–5 µm. The detection limits of analyzed elements, including Na, Mg, Al, Si, K, Ca, Mn, Fe, F, Cl were better than 0.1 wt%. The signal acquisition and background counting times for elements were 15 and 5 s, respectively. Matrix corrections were performed by the ZAF procedures (Jurek and Hulínský, 1980).

In situ trace element analyses of magnetite were performed by Laser Ablation Inductively-Coupled Plasma Mass Spectrometry (LA-ICP-MS) on polished thick sections at the Mineral Geochemistry Laboratory, Ore Deposit and Exploration Centre (ODEC), Hefei University of Technology, China. The analyses were carried out on an Agilent 7900 Quadrupole ICP-MS coupled to a Photon Machines Analyte HE 193-nm ArF Excimer Laser Ablation system. A squid signal smoothing device is included in this laser ablation system. Helium was used as the carrier gas, and argon was used as the make-up gas and mixed with the carrier gas via a T-connector before entering the ICP (Ning et al., 2017; Wang et al., 2017). Each analysis was performed using a uniform spot diameter of 30 mm at 8 Hz with energy of ~ 4 J/cm² for 40 s after measuring the gas blank for 20 s. The following basic set of isotopes for magnetite were monitored: ²⁵Mg, ²⁷Al, ²⁹Si, ⁴³Ca, ⁴⁵Sc, ⁴⁹Ti, ⁵¹V, ⁵³Cr, ⁵⁵Mn, ⁵⁷Fe, ⁵⁹Co, ⁶⁰Ni, ⁶⁵Cu, ⁶⁶Zn, ⁷¹Ga, ⁷⁴Ge, ⁸⁵Rb, ⁸⁸Sr, ⁸⁹Y, ⁹⁰Zr, ⁹³Nb, ⁹⁵Mo, ¹¹⁸Sn, ¹³⁷Ba, ¹⁷⁸Hf, ¹⁸¹Ta, ¹⁸²W, ²⁰⁸Pb, ²⁰⁹Bi, ²³²Th, ²³⁸U.

Standard reference materials GSE-1G, GSD-1G, BCR-2G and NIST 610 were used as external standards to plot the calibration curve. The preferred values of element concentrations for the USGS reference glasses are from the GeoReM database (<http://georem.mpch-mainz.gwdg.de/>). Standard reference materials were run after each 10–15 unknowns; detection limits were calculated for each element in each spot analysis. The off-line data processing was performed using a program called ICPMSDataCal (Liu et al., 2008). Oxide minerals were calibrated against multiple reference materials without applying internal standardization. Analytical errors for most major and trace elements are 5% and 10%, respectively. The results for major elements for magnetite are consistent with the EPMA data at 5% analytical error.

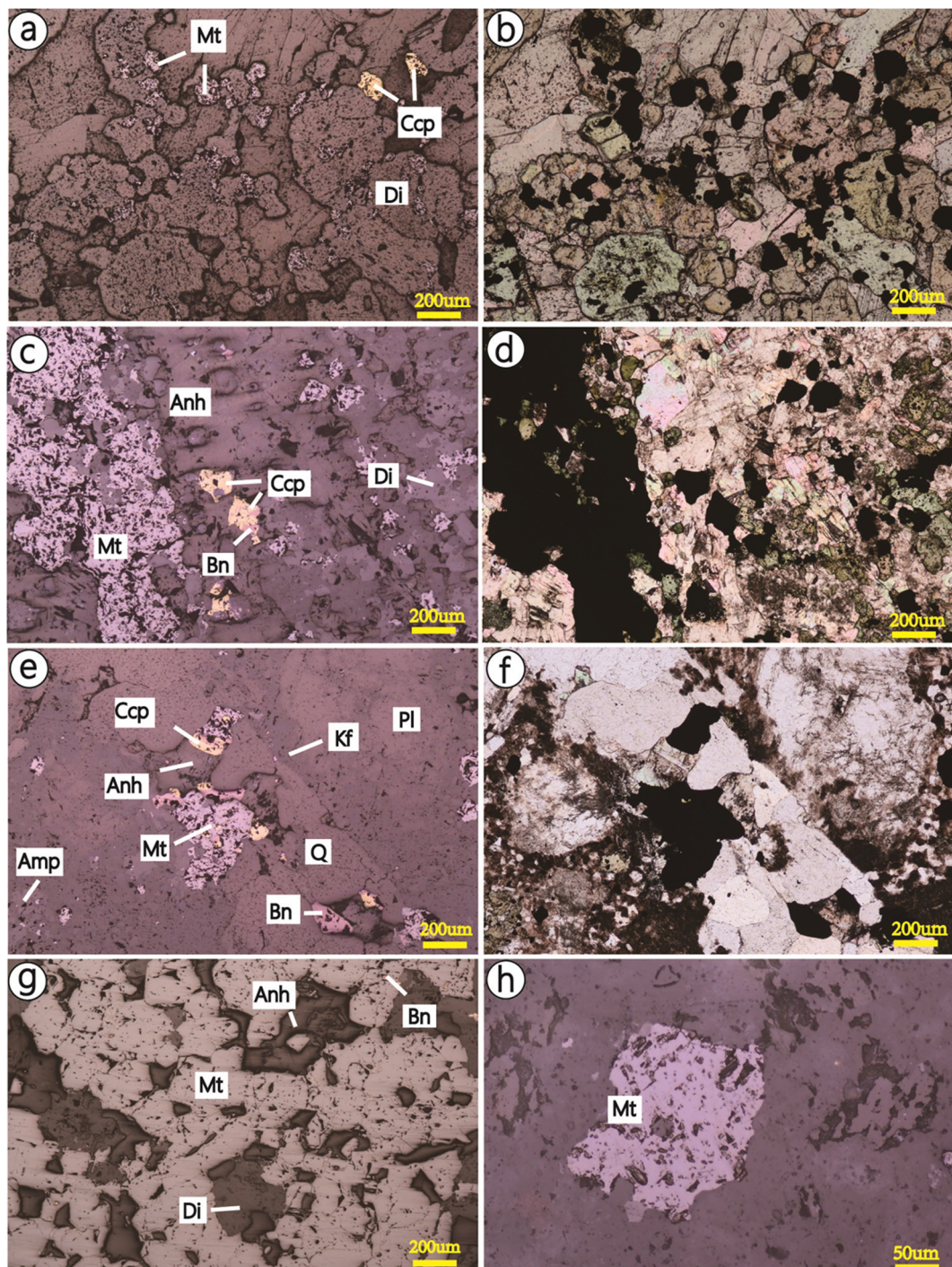


Fig. 5. Examples of magnetites selected for the study from Chating deposit. a, b: Sparsely disseminated magnetite in exoskarn; c, d: Coarse magnetite in endoskarn overlapped by later copper mineralisation; e, f: Q-Mt-Ccp-Bn-Anh-Kf vein in potassium alteration; g: Coarse magnetite in Q-Mt-Act-Dio vein from sodic-calcic alteration; h: Magmatic magnetite in quartz diorite porphyry. a, c, e, g, h are reflected light and b, d, f are plane polarized light.

5. Results

Only Mg, Al, Si, Ca, Ti, V, Cr, Mn, Co, Ni, Zn, Mo, Ga and Sn in magnetite occur at levels above the detection limit in LA-ICP-MS analysis, and SiO_2 , Al_2O_3 , TiO_2 , K_2O , Na_2O , FeO^T , MnO , MgO , CaO , Na_2O ,

K_2O , F and Cl in biotite were analyzed by EMPA. In Appendix I and II, we present the analytical results above the detection limit obtained by EMPA and LA-ICP-MS on different minerals. Magmatic biotite data were cited from Xiao et al. (2018 submitted).

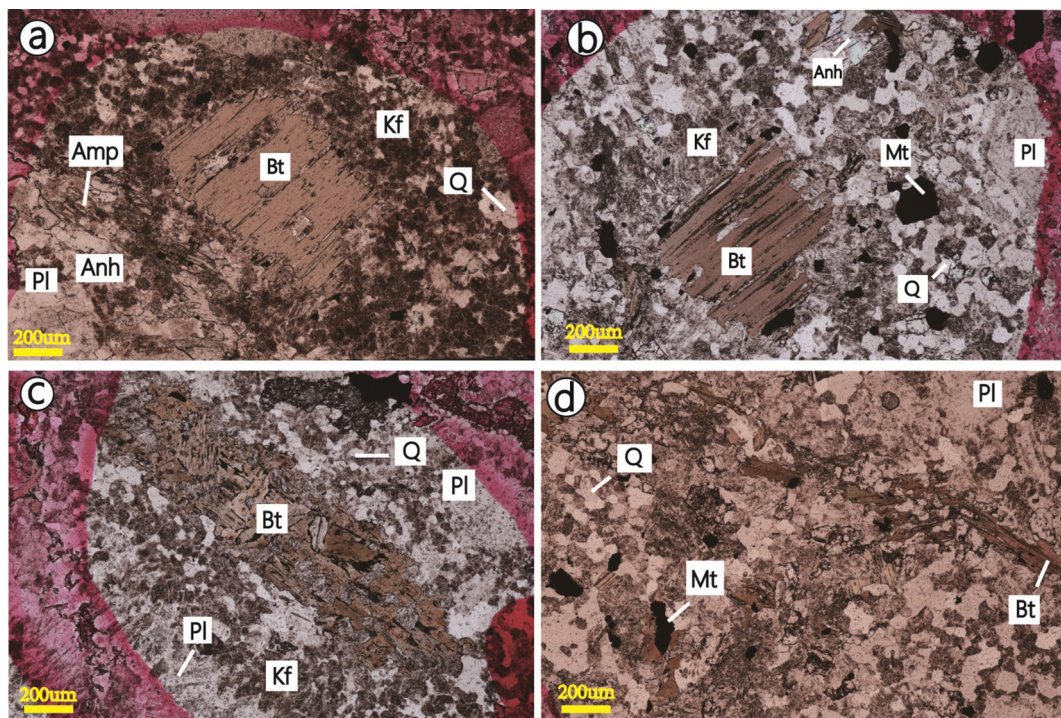


Fig. 6. Plane polarized light photos of different types of biotite. a, b: Magmatic biotite in quartz diorite porphyry; c: Hydrothermal biotite replacing amphibole; d: Vein-type biotite in the potassic alteration zone.

5.1. Magnetite composition

Magmatic magnetites from the quartz diorite porphyry have the highest V and Cr, high Mn and Zn, and lower Al than hydrothermal magnetites in the potassic and sodic-calcic alteration (Fig. 7b, e-g). Magnetites from exoskarn show distinctly different characteristics from others. They have the lowest Ti, V, Ni, Mo and Co (Fig. a, b, h, i), but highest Mg, Mn, and Zn (Fig. 7d, g, j). However, magnetites from endoskarn have higher V, Mo, Co and lower Mg and Mn than magnetites from exoskarn, but Ti in endoskarn is elevated (up to 4921 ppm; Fig. 7a-f). Magnetites from sodic-calcic alteration have similar average contents of V, Cr, Ni, Mn, Zn, Ga, Sn and Mo, with higher Ti and Al, and lower Co than magnetites from potassic alteration (Fig. 7a-f). Almost all the elements in magnetite from potassic alteration have wider ranges than those in sodic-calcic alteration. Ca and Si content in all types of magnetite have wide ranges extending over several orders of magnitude.

5.2. Biotite composition

Magmatic and hydrothermal biotites show distinctly different compositions. Magmatic biotites from quartz diorite porphyry have higher Al_2O_3 , K_2O , Na_2O , TiO_2 , FeO^T , MnO and Cl , but lower MgO , CaO and SiO_2 than biotites from potassic alteration (Fig. 8a-i, k). The two different types of biotite have similar but variable F contents (Fig. 8j). Hydrothermal biotites have a wider range of SiO_2 , TiO_2 , MgO , CaO and K_2O contents, and negative variation trends between MgO and TiO_2 , FeO^T and MgO , and FeO^T and TiO_2 , indicate wide isomorphic substitution. The negative variation trend between MgO and Cl , and FeO^T and F may be caused by “Mg-Cl avoidance” and “Fe-F avoidance” (Muñoz, 1984). Compared to F (average 0.13 wt%), the Cl content

(average 0.22 wt%) is higher in magmatic and hydrothermal biotites (Fig. 8j, k). In contrast to magmatic and hydrothermal biotite from typical porphyry deposits, hydrothermal biotite in Chating shows similar variation ranges to biotite from the potassic zone, apart from SiO_2 , MnO and CaO , which are similar to biotite from the phyllitic zone. MnO in magmatic biotite from Chating is much higher than in biotites from typical porphyry copper deposits (Fig. 8a-i).

We calculated the crystal-chemical formula on the basis of 22 oxygen atoms. The Fe^{3+} and Fe^{2+} were calculated using the method of Dymek (1983). The sums of Si + Al in the two types of biotite are < 4, indicating additional Fe^{3+} should occur in the tetrahedral site, and biotites in Chating plot in the Mg biotite field of the $\text{Mg}-\text{Fe}^{3+} + \text{Ti} + \text{Al}^{\text{VI}}-\text{Fe}^{2+} + \text{Mn}$ ternary diagram (Fig. 9a). In the $10^*\text{TiO}_2-\text{FeO}_{\text{total}} + \text{MnO}-\text{MgO}$ ternary diagram (Fig. 9b) (Nachit et al., 1985, 2005), all of the hydrothermal biotites plot in the reequilibrated biotite field, and most of the magmatic biotites plot in the primary magmatic biotite field, possibly indicating that hydrothermal alteration overprinted some magmatic biotite. Based on the petrographic characteristics, we concluded that the intensity of hydrothermal alteration was not enough to change the relationship between magmatic and hydrothermal biotite.

The fluorine intercept IV(F), chlorine intercept IV(Cl), and F/Cl intercept IV(F/Cl) values are important physicochemical parameters to describe the relative F and Cl contents in micas; these values are defined by Muñoz (1984) as:

$$\text{IV}(F) = 1.52X_{\text{Mg}} + 0.42X_{\text{An}} + 0.2X_{\text{sid}} - \log(X_F/X_{\text{OH}})$$

$$\text{IV}(Cl) = -5.01 - 1.93X_{\text{Mg}} - \log(X_{\text{Cl}}/X_{\text{OH}})$$

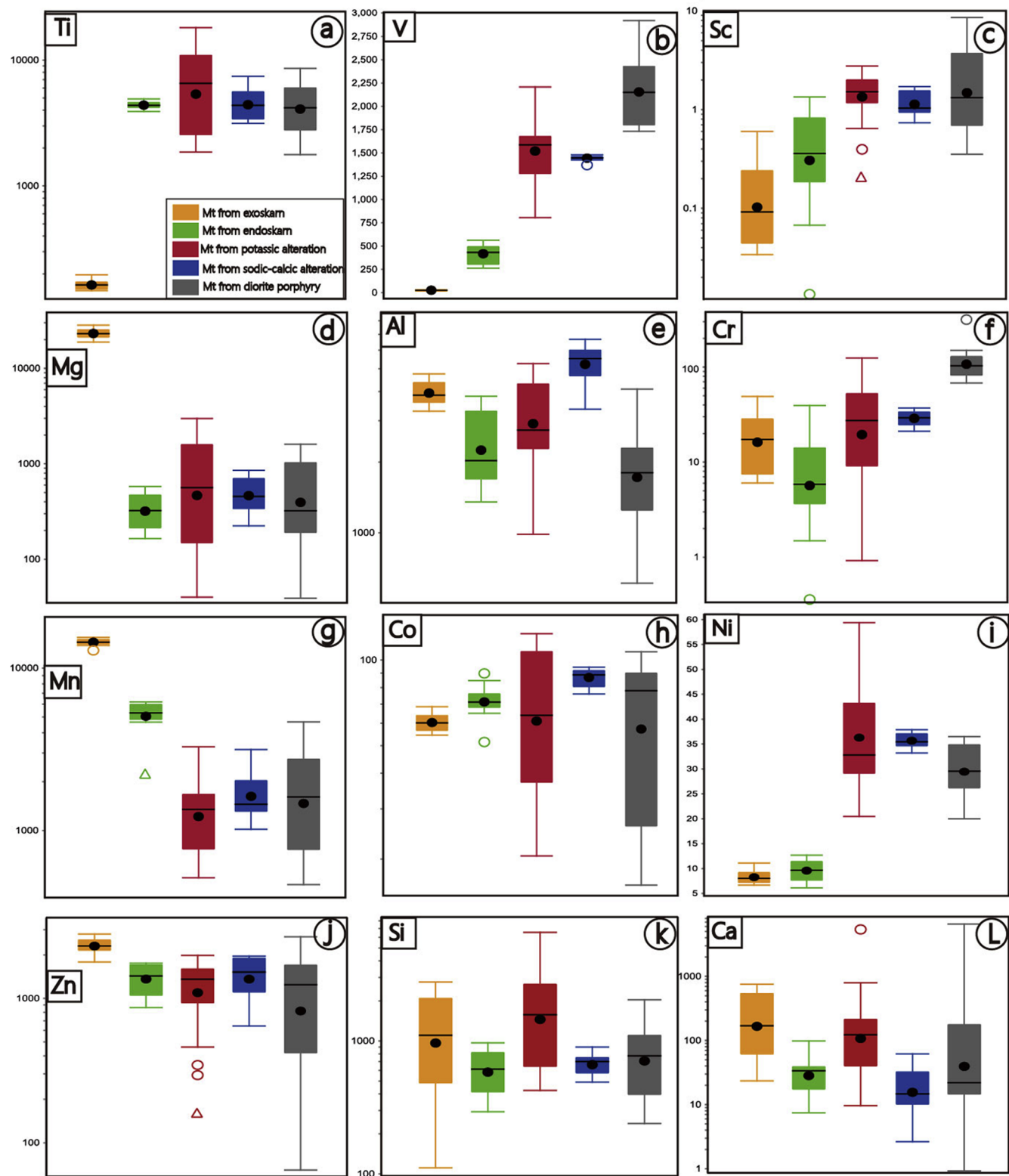


Fig. 7. ‘Box-and-whisker’ plots of element contents for magnetite. (a) Ti, (b) V, (c) Sc, (d) Mg, (e) Al, (f) Cr, (g) Mn, (h) Co, (i) Ni, (j) Zn, (k) Si, (l) Ca. The box encompasses the median (black line), average (solid black circle) and is bounded by the upper and lower quartiles, with the lines showing 95% of all data for that sample. Outliers are shown by open circles.

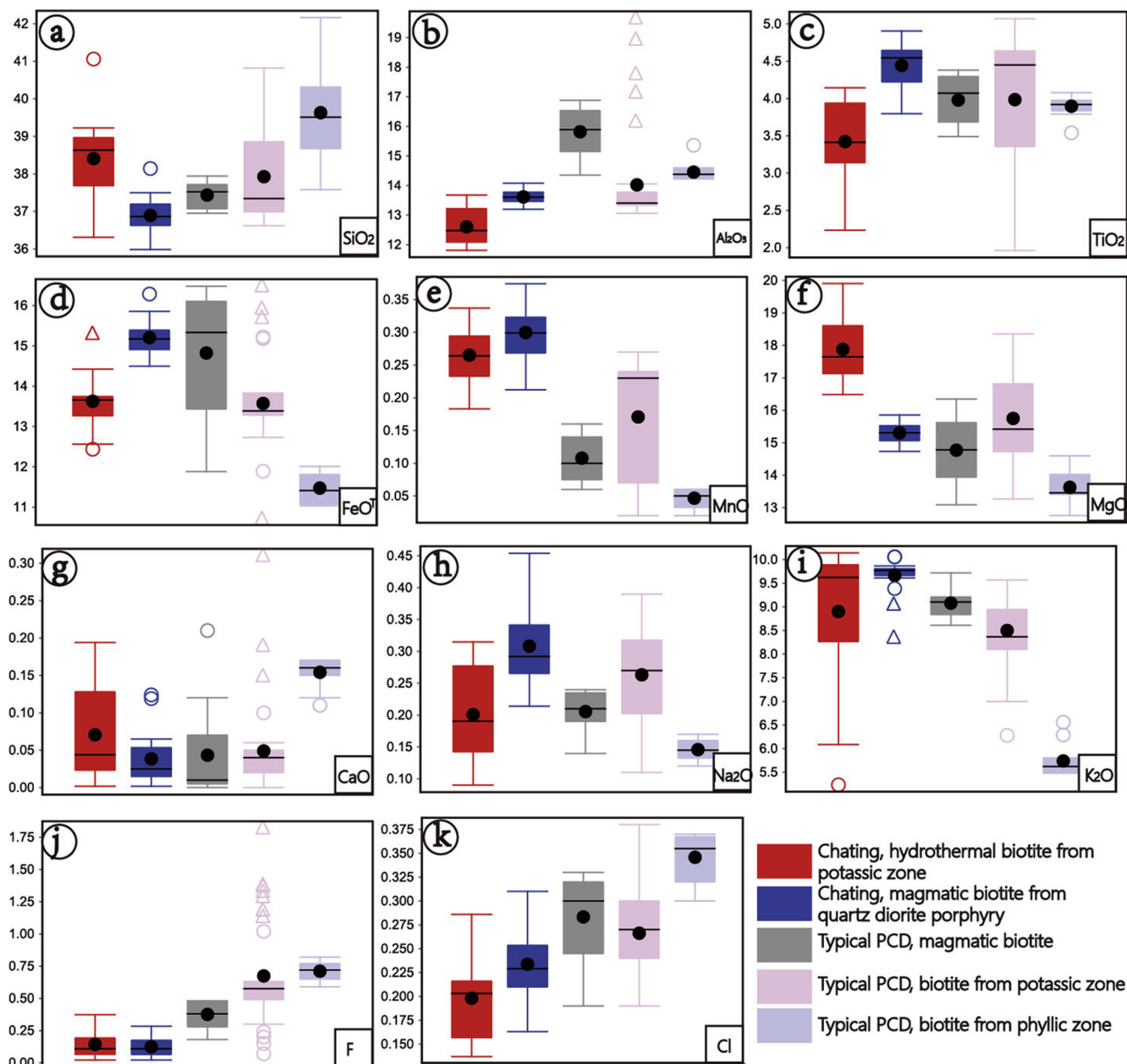


Fig. 8. ‘Box-and-whisker’ plots of elements content for different biotite from Chating and typical porphyry deposits. (a) SiO_2 , (b) Al_2O_3 , (c) TiO_2 , (d) FeOT , (e) MnO , (f) MgO , (g) CaO , (h) Na_2O , (i) K_2O , (j) F , (k) Cl . (Biotite data for typical porphyry deposits quoted from Afshooni et al., 2013; Ayati et al., 2008; Boomeri et al., 2009; Parsaapoor et al., 2015).

$$\text{IV}(\text{F}/\text{Cl}) = \text{IV}(\text{F}) - \text{IV}(\text{Cl})$$

where $X_{\text{Mg}} = \text{Mg}/\text{sum of octahedral cations}$, $X_{\text{An}} = 1 - (X_{\text{Mg}} + X_{\text{sid}})$, $X_{\text{sid}} = (3 - \text{Si}/\text{Al}) / 1.75 - (1 - X_{\text{Mg}})$, and X_{F} , X_{Cl} and X_{OH} are the mole fractions of F, Cl, and OH in the hydroxyl site.

Magmatic and hydrothermal biotites in Chating have similar IV(F) (2.73 to 3.95) and IV(Cl) (-4.42 to -4.09) to the intercept values of biotites from worldwide porphyry copper deposits; IV(F) (1.1 to 3.0), IV(Cl) (-5.0 to -2.7) (Fig. 10). However, the values of IV(F/Cl) in Chating are 6.96 to 8.13, higher than typical porphyry copper deposits (IV(F/Cl) 4.60 to 7.0) (Loferski and Ayuso, 1995; Munoz, 1984; Selby and Nesbitt, 2000; Taylor, 1983).

6. Discussion

6.1. Physicochemical conditions in magmatic-hydrothermal processes

6.1.1. Temperature, pressure and composition

In magmatic rocks the content of Al and Ti in magnetite shows a positive relationship with temperature, and vary by about one order of magnitude (Nielsen et al., 1994; Toplis and Carroll, 1995). In hydrothermal systems, Al and Ti in magnetite also show a positive relationship with temperature, however, their contents can vary by several orders of magnitude (Nadol and Koenig, 2011, 2014; Ray and Webster, 2007). Concentrations of Ti + V, Al + Mn, Sn and Ga also show

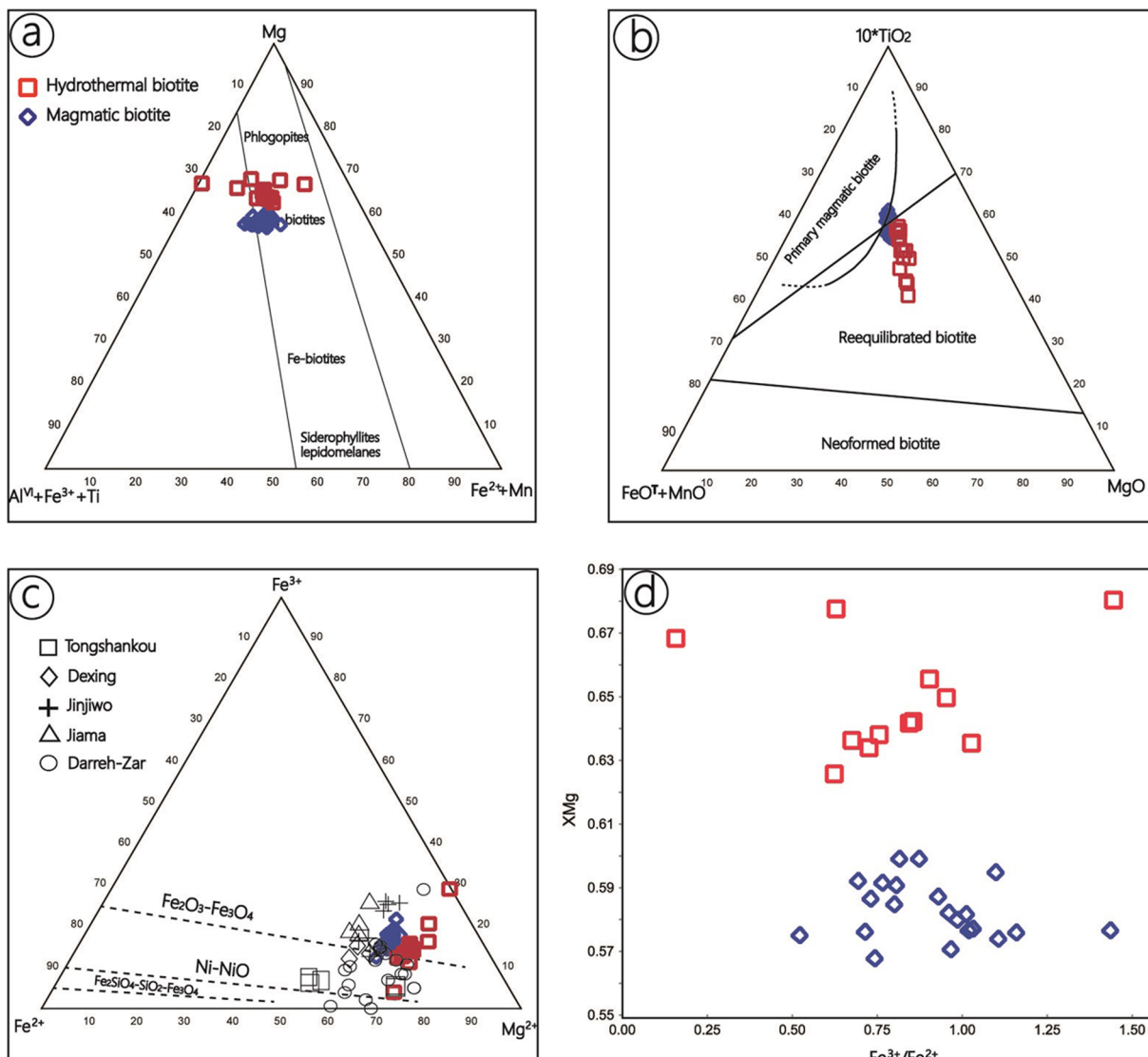


Fig. 9. (a) Ternary diagram $\text{Fe}^{3+} + \text{Al}^{\text{VI}} + \text{Ti-Fe}^{2+} + \text{Mn-Mg}$ for biotite (Foster, 1960); (b) Ternary diagram $10^*\text{TiO}_2-\text{FeO}^T + \text{MnO-MgO}$ for biotite (Nachit et al., 1985, 2005); (c) Ternary diagram $\text{Fe}^{2+}-\text{Mg}^{2+}-\text{Fe}^{3+}$ for biotite (modified by Wones et al., 1965); Biotite data for other porphyry copper deposits quoted from Tang et al., 2016; Liu et al., 2010; Du et al., 2017; Jiang, 2004; Parsaipoor et al., 2015); (d) Binary plots of $\text{Fe}^{3+}/\text{Fe}^{2+}$ vs. X_{Mg} for biotite.

positive correlations with temperature (Nadol et al., 2014a,b); by contrast, elements such as Cu, Zn and Mn are expected to be enriched in fluids at lower temperature (Ilton and Eugster, 1989).

In general, magmatic magnetites have high Ti contents, consistent with our observations at Chatting (Fig. 7a). Hydrothermal magnetites from skarns at Chatting have high Mg, Mn, Zn and Al, low V and Ti (but Ti content in magnetite from endoskarn is much higher than from exoskarn), whereas magnetites from potassic and sodic-calcic alteration have high Ti and V, and low Mn, Al, and Zn. There are no obvious correlations in plots of Ti versus Al, Al + Mn versus Ti + V and Sn versus Ga (Fig. 11a-c), which suggests that temperature may not be the main controlling factor for Ti, Al, Mn, Zn, Sn, and Ga contents in hydrothermal magnetites.

The Ti content in biotite also increases with increasing temperature (Robert et al., 1976; Wones et al., 1965). Magmatic biotites in Chatting has higher Ti content than hydrothermal biotites (Fig. 8c), which is consistent with its higher formation temperature in the magmatic

system. Al content in magmatic biotite increases with increasing pressure; using the geobarometry of Al in biotite, $P = 3.03^*\text{Al} - 6.53 (\pm 0.33)$ (Uchida et al., 2007), we calculated pressure of 44–88 MPa for magmatic biotite. The Al content in hydrothermal biotite is much lower than in magmatic biotite, which may indicate a pressure drop from magma to hydrothermal fluid (Fig. 8b).

In contrast to magmatic systems, almost all of the elements in hydrothermal biotite and most of the elements in hydrothermal magnetite (especially Mg, Al, V, Cr, Mn and Zn) have a wider range (Fig. 8a-k), which indicates variable fluid compositions because the fluid composition always provides a first order control on minor and trace element concentrations in hydrothermal systems (Nadol et al., 2014a,b). Temperature and pressure decrease may have resulted in early fluid release from the magma, and hydrothermal magnetite and biotite precipitated from an environment with unstable fluid compositions.

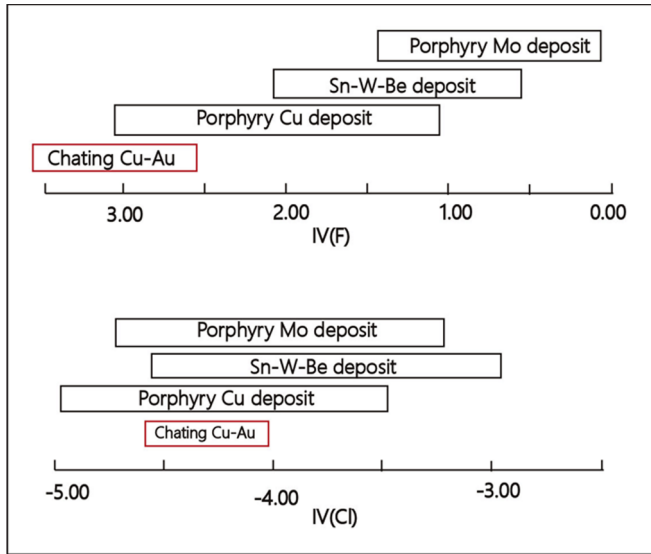


Fig. 10. Comparison of IV(F) and IV(Cl) between Chating and porphyry Cu deposits, porphyry Mo deposits and Sn-W-Be deposits (modified from Muñoz, 2014).

6.1.2. Redox conditions

The content in magnetite of elements with variable valence is strongly controlled by the redox conditions of the magma or hydrothermal fluid. For example, compared to V^{4+} and V^{5+} , V^{3+} is more compatible with the spinel structure of magnetite (Balan et al., 2006; Righter et al., 2006a, b; Toplis and Corrigan, 2002), and minor changes in redox conditions lead to changes in the partition coefficient for V between magnetite and hydrothermal fluid; therefore the V content in magnetite is a good indicator of changes in redox conditions. In Chating deposit, the V content in magnetite decreases from magma to hydrothermal alteration stages, indicating an initial increase of f_{O_2} from magma to hydrothermal fluids, which thereafter fluctuate in f_{O_2} (Fig. 7b). Notably, V in magnetite from skarn is much lower than in other magnetites. The f_{O_2} drop from skarn to potassic alteration may have resulted in precipitation of chalcopyrite and bornite in potassiac alteration due to availability of reduced sulfur by sulfate reduction.

X_{Mg} in magmatic biotite is lower than in hydrothermal biotite, and Fe^{3+}/Fe^{2+} and X_{Mg} in hydrothermal biotite also show a wider range (Fig. 9d), indicating lower f_{O_2} for the magmatic biotite (Wones et al., 1965) and higher and fluctuating f_{O_2} for hydrothermal biotite, which is consistent with the results from magnetite. In the ternary diagram $Fe^{2+}-Fe^{3+}-Mg^{2+}$, two types of biotites plotted near the hematite-magnetite buffer zone (Fig. 9c), manifesting very high f_{O_2} in magmatic

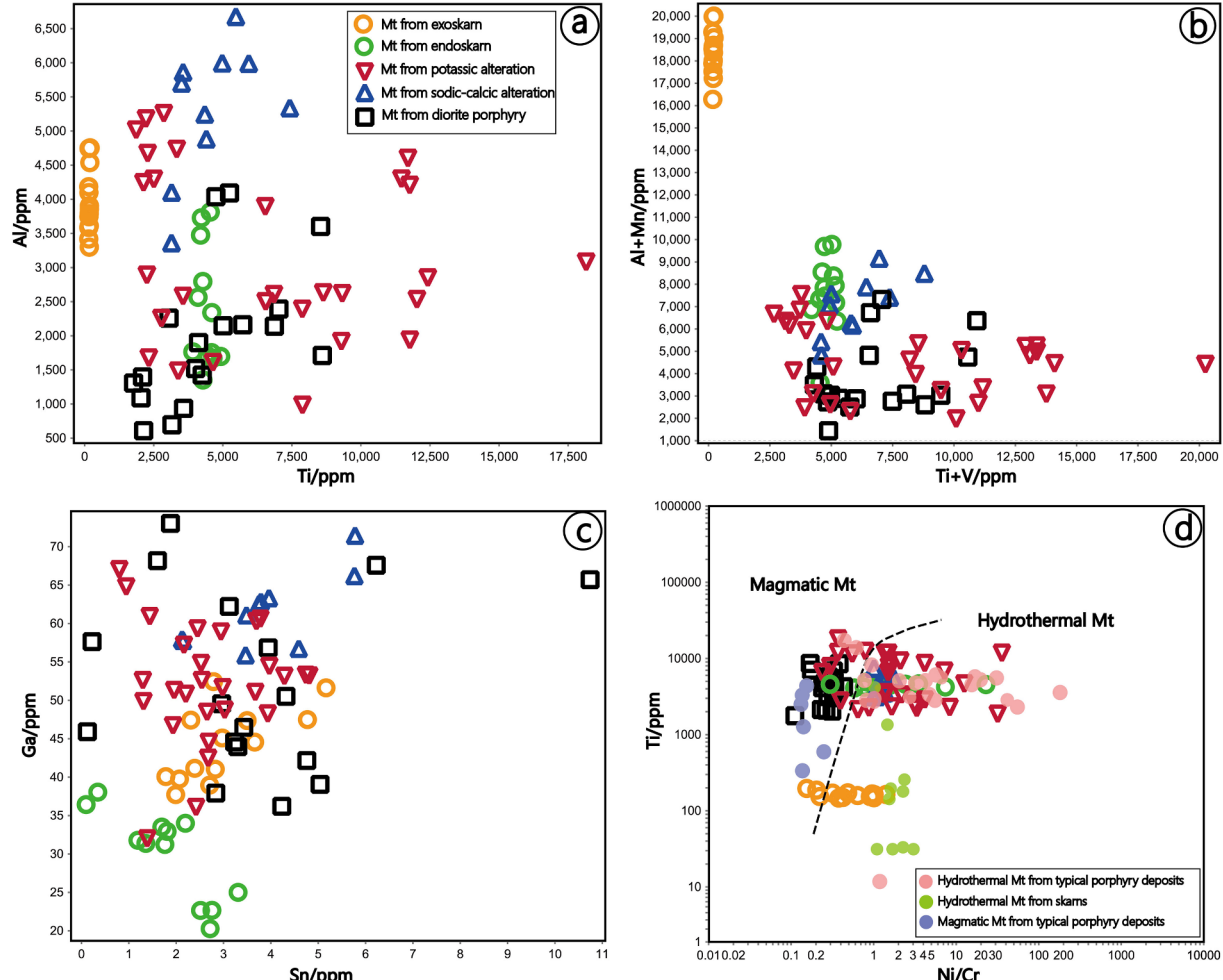


Fig. 11. Binary plots of selected trace elements in magnetite from Chating. (a) Ti vs. Al; (b) Ti + V vs. Mn + Al; (c) Sn vs. Ga; (d) Ni/Cr vs. Ti (modified from Dare et al., 2014; magnetite data for typical porphyry and skarn deposits quoted from Dare et al., 2014; Canil et al., 2016) for different types of magnetite.

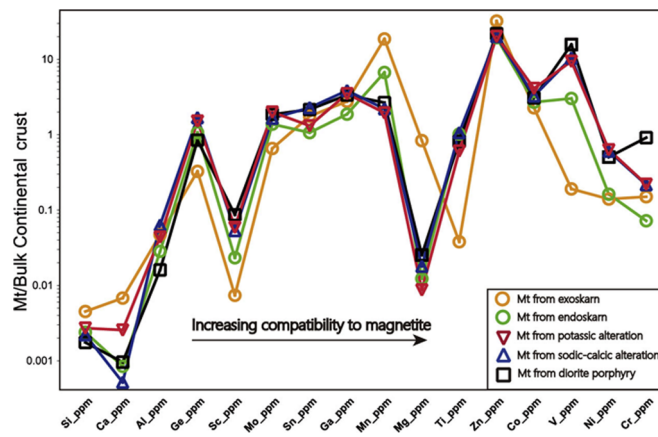


Fig. 12. Multielement variation diagram for magnetite, normalized to bulk continental crust (values from Rudnick and Gao, 2003).

hydrothermal processes, which is consistent with most typical porphyry deposits. Also, there is a wider range of $\text{Fe}^{3+}/\text{Fe}^{2+}$ in hydrothermal biotite, indicating fluctuating oxygen fugacity.

Porphyry copper deposits are related to magmas with high oxygen fugacity (Sillitoe, 2010), and the optimal initial oxygen fugacity for porphyry Cu deposits is between the nickel-nickel oxide (NNO) and hematite-magnetite (HM) buffers, with pH between 7 and 10 (Pokrovski and Dubrovinsky, 2011; Sun et al., 2003). In Chating, the f_{O_2} of magma and fluids reached the HM buffer, as revealed by biotite geochemistry, and there was high pH when potassio alteration formed (Seedorff et al., 2005), which means that Chating met the optimal oxygen fugacity and pH conditions to form a porphyry copper deposit.

In summary, there was a drop in temperature and pressure and an increase in f_{O_2} from the magmatic to hydrothermal stages, and temperature and pressure stayed at a constant level during the hydrothermal mineralization stages, whereas the f_{O_2} fluctuated when potassio, sodic-calcic and skarn alteration formed, based on Ti, Al, V, Zn, Mn, Sn, and Ga in magnetite and Al, $\text{Fe}^{3+}/\text{Fe}^{2+}$, X_{Mg} in biotite. Variable major and minor element compositions in magnetite and biotite demonstrate unstable fluid compositions during hydrothermal mineral deposition.

6.2. Implications for ore genesis

6.2.1. Fluid source

We observe that different magnetites from different types of alteration have different element compositions, which may have resulted from changes in fluid composition, and/or fluid conditions (P, T, pH, f_{O_2} , etc). As noted previously, changes in chemical composition of the fluids appear to be the main cause of the observed changes in magnetite composition; these, in turn, may result from different fluid sources, or from modifications to fluid chemistry, e.g., by wallrock interaction.

The Ti-Ni/Cr diagram can effectively distinguish magnetite formed in magmatic and hydrothermal environments (Dare et al., 2014). In Chating, > 95 percent of hydrothermal magnetites plotted in the hydrothermal magnetite field and have Ti contents similar to hydrothermal magnetites from typical porphyry deposits (Fig. 11d). Moreover, increasing Ni/Cr ratios for hydrothermal magnetites from Chating trend into the magmatic magnetite field, indicating a magmatic origin for the hydrothermal fluids (Dare et al., 2014). In the average multielement variation diagrams for magnetite (normalized to bulk continental crust; Fig. 12), magnetites from potassio and sodic-calcic alteration have a similar trend to magmatic magnetites, which also indicates a dominantly magmatic hydrothermal fluid origin.

Magnetites from potassio alteration have element concentrations, especially in Ti, V, Al, Mg, Mn, Ga, Sn, Si and Ca, that are more variable than magnetites in sodic-calcic alteration; this implies significantly different fluid chemistry between potassio and sodic-calcic alteration (Fig. 7a, b, d, e, g, k, l; Fig. 11c). The origin of fluids responsible for sodic-calcic alteration is controversial, whether from magmatic aqueous fluids, external brine, or a mixture of the two; by contrast, potassio alteration has a magmatic-hydrothermal fluid origin (Carten, 1986; Dilles and Einaudi, 1992, 1995; John, 1989; Seedorff et al., 2005, 2008; Sillitoe, 2010). In general, Ti and Al are much higher in magmatic magnetite because of the higher forming temperature and melt compositions; Mg, Mn, Si and Ca can be enriched in hydrothermal fluids due to high fluid/rock interactions (Einaudi et al., 1982; Meinert, 1987); Sn and Ga contents relate to temperature, and high Sn and Ga contents may imply a magmatic-hydrothermal source (Nadol et al., 2014a,b). In Chating, magnetites from sodic-calcic and potassio alteration show high and variable ranges of Ti, Al, Ga, Sn, Mg and Mn contents that are similar to those of magmatic magnetite, suggesting a predominately magmatic-hydrothermal fluid origin. Magnetites from potassio alteration have higher and much more variable contents of Mg, Mn, Si and Ca

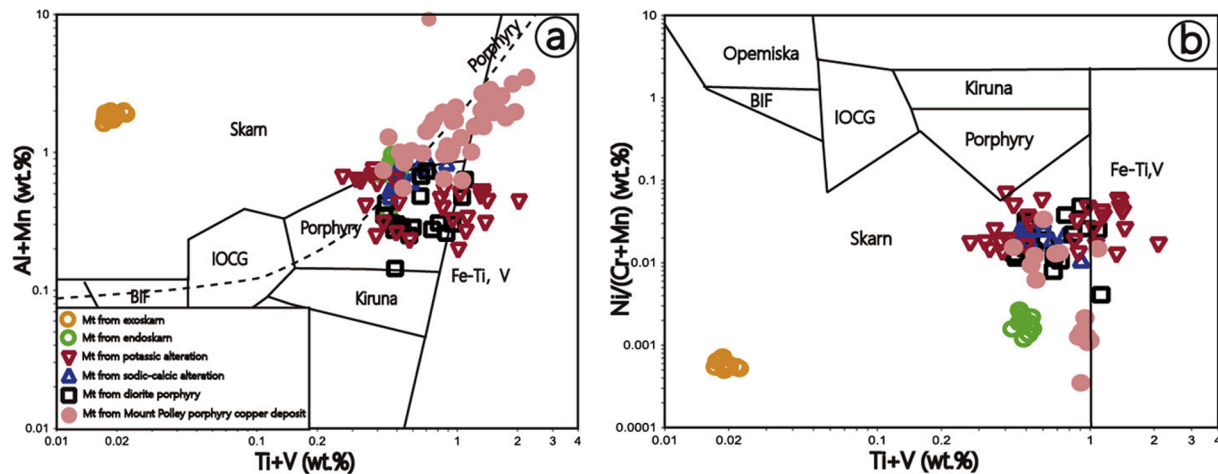


Fig. 13. Discrimination diagrams for different types of magnetite. (a) Plot of $(\text{Al} + \text{Mn})$ vs. $(\text{Ti} + \text{V})$ (modified from Dupuis and Beaudoin, 2011); (b) Plot of $\text{Ni}/(\text{Cr} + \text{Mn})$ (wt%) vs. $(\text{Ti} + \text{V})$ (modified from Nadoll et al., 2014; data for Mt. Polley quoted from Canil et al., 2016).

than magnetites from sodic-calcic alteration, suggesting addition of an external fluid.

Skarn magnetites have apparently different chemistry characteristics from magmatic magnetites and other types of hydrothermal magnetites, which maybe indicate a mainly exotic fluid origin. In Chating, the host rocks for magnetites from exoskarn are mainly Triassic carbonates, whereas the other three types of magnetite have the same wall rock (quartz diorite porphyry). Magnetites inherit compositional features of wall rocks or primary minerals that have been replaced (Einaudi et al., 1982; Meinert, 1987; Nadoll et al., 2015). We find that the magnetites from skarn have much higher Mg, Mn and Zn, and lower V contents than magnetites from potassic and sodic-calcic alteration (Fig. 7b, d, g, j), which implies a stronger fluid-rock interaction has happened for skarns. Si, Ca and Co/Ni in magnetites from skarn are higher and more variable than in potassic and sodic-calcic alteration (Fig. 7k, l, Appendix 2), which also indicates stronger fluid-rock interaction in skarns (Bajwah et al., 1987; Nadoll et al., 2011; Zhou et al., 2015).

Biotite chemistry also provides information on fluid origins. When compared to different types of biotite from typical porphyry Cu deposits, hydrothermal biotite in Chating shows element contents such as Al_2O_3 , TiO_2 , FeO^T , MgO , Na_2O that are similar to biotites from the potassic zone, whereas SiO_2 and CaO contents are high and have a range similar to but more variable than biotite from the phyllitic zone (Fig. 8a-i). Potassic and phyllitic alteration in porphyry systems is mainly produced by magmatic-hydrothermal fluids (Sillitoe, 2010; Seedorff et al., 2005), but meteoric water may have mixed with late stage magmatic fluids to produce phyllitic alteration. Hydrothermal biotites from Chating are similar in composition to biotites from potassic alteration zones in porphyry deposits, but have elevated Ca and Si, more similar to biotites in the phyllitic zone of porphyry deposits. This possibly indicates addition of external fluids rich in Ca and Si from carbonate wall rock to the magmatic hydrothermal system.

Magmatic and hydrothermal biotites from Chating have similar and scattered IV(F) and IV(Cl) values (Fig. 10), and the values are similar to worldwide porphyry copper deposits that formed in magmatic arc settings (Loferski and Ayuso, 1995; Munoz, 1984; Selby and Nesbitt, 2000; Taylor, 1983), indicating a predominately magmatic fluid source. High IV(F) values and low IV(Cl) values in different types of biotite demonstrate that the magmatic-hydrothermal system in Chating was enriched in Cl and lacked F, which is significant as abundant Cl plays an important role in the transport of Cu (Parsapoor et al., 2015; Li et al., 2011).

Based on the geochemistry of different types of magnetite and biotite at Chating deposit we conclude that there was a predominately magmatic origin for fluids responsible for early stage potassic and sodic-calcic hydrothermal alteration, but there is evidence to suggest mixing of magmatic and external fluids during the skarn and potassic alteration.

6.2.2. Deposit genesis

Chating is a Cu-Au deposit in which widespread potassic and phyllitic alteration developed with stockwork sulfide mineralization. Skarn alteration also occurred in the deposit, but it lacks copper mineralization. In this study, we use several discrimination diagrams to provide information on ore genesis.

In the plot of Ti + V against Al + Mn, magnetite from the exoskarn occurs in the skarn field, whereas part of the magnetite from the endoskarn occurs in the porphyry field, and most of the magnetite from potassic and sodic-calcic alteration occurs in the porphyry area (Fig. 13a), suggesting Chating is a porphyry type deposit. However, in the plot of Ni/(Cr + Mn) against Ti + V, the low Ni/(Cr + Mn) ratio

results in all the magnetite occurring in the skarn area (Fig. 13b), but there is an increasing trend in Ni/(Cr + Mn) ratios in magnetites from skarn, to potassic, to sodic-calcic alteration. Comparing magnetite geochemistry in Chating with some typical porphyry copper deposits from southwestern USA and Canada, we found that magnetites in Chating show a range of element contents similar to Mt. Polley porphyry Cu-Au deposit, especially the high Mn which caused the low Ni/(Cr + Mn). In this case, the binary diagram of Ti + V vs. Ni/(Cr + Mn) is not appropriate to discriminate the deposit type (Pisiak et al., 2017).

Biotite geochemistry from Chating also shows high Mn contents, in contrast to biotite from typical porphyry deposits (Fig. 8e). Pass (2014) considered that carbonate assimilation prior to mineralization played an important role in the mineralization in Mt. Polley porphyry Cu-Au deposit, based on the S, C-O, Pb and Sr isotope data from different mineralization stages; high Mn in magnetite is controlled by fluid acidity and chlorinity (Ilton and Eugster, 1989; Canil et al., 2016). As discussed above, addition of external fluids to the dominant magmatic-hydrothermal fluid cannot be excluded, and biotite geochemistry also indicated Cl-enrichment and a lack of F in the magmatic-hydrothermal system at Chating. We conclude that inherited characteristics from carbonate wall rocks and a Cl-enriched system may have resulted in the high Mn in the magmatic-hydrothermal system at Chating; magmatic and hydrothermal magnetite and biotite with high Mn contents deposited in the Mn- and Cl-enriched environment. The similarity of IV(F) and IV(Cl) values in biotites at Chating to values reported for worldwide porphyry deposits support that Chating has porphyry deposit affinities.

7. Conclusions

Magmatic and hydrothermal magnetites and biotites from Chating Cu-Au deposit show distinct geochemical characteristics. Different magnetites can be distinguished by Ti, V, Al, Sn, Ga, Zn, Ni/Cr, Mg and Mn, and different biotites can be distinguished by TiO_2 , Al_2O_3 , FeO^T , MgO , SiO_2 , CaO , and Cl.

Geochemistry of different types of magnetites and biotites indicate that the host quartz diorite porphyry was emplaced at shallow depths (1.7–3.3 km). Release of magmatic-hydrothermal fluids resulted in a drop in temperature and pressure but an increase in $f\text{O}_2$ from the magma to the hydrothermal fluids. $f\text{O}_2$ increased from potassic and sodic-calcic to skarn alteration in the hydrothermal stages, which may have been caused by variations in fluid compositions.

Discrimination diagrams such as IV(F) versus IV(Cl) for biotite and Ni/Cr versus Ti, and Al + Mn versus Ti + V for magnetite indicate that there was a predominately magmatic fluid origin, but Mg, Mn, Si, Ca and Co/Ni ratio in magnetite and high SiO_2 , CaO and MnO in biotite indicate addition of external fluids to the hydrothermal system, especially for the potassic and skarn alteration. This differs from porphyry deposits developed in subduction-related magmatic arcs. Chating deposit shows affinities to porphyry-type Cu-Au systems, but was affected by external fluids during its evolution.

Acknowledgments

We thank Shilong Qian and Qianguo Yang from No.322 Unit of Bureau of Geology and Mineral Exploration of Anhui Province for their valuable support during the field work and Juan Wang from Hefei University of Technology for the electron probe microanalysis. This work was financially supported by the National Key Research and Development Program of China (2016YFC0600206) and Natural Science Foundation of China (grants 41320104003).

Appendix A

See Table A1.

Table A1
Major and trace element concentrations in magnetite analyzed by LA-ICP-MS.

Type	Sample	FeO/wt%	Mg/ppm	Al/ppm	Si/ppm	Ca/ppm	Sc/ppm	Ti/ppm	V/ppm	Cr/ppm	Mn/ppm	Co/ppm	Ni/ppm	Zn/ppm	Ga/ppm	Ge/ppm	Mo/ppm	Sn/ppm	Co/Ni
D.L.																			
Mt from exoskarn	M-1614-1	0.005%	2.32	1.59	385.07	96.37	0.28	3.93	0.1	2.81	1.04	0.08	1.5	2.6	0.29	0.73	0.27	0.97	
Mt from exoskarn	M-1614-1	90.22	24090.05	4754	843.65	0.26	196.63	26.0	49.02	14283.42	60.15	7.56	2302.3	52.44	0.41	2.79	0.41	8.0	
Mt from exoskarn	M-1614-1	89.89	26049.04	4099	1102.59	499.90	0.43	153.91	25.4	107.5	1434.11	59.86	9.76	2359.6	47.50	0.38	4.77	6.1	
Mt from exoskarn	M-1614-1	89.90	27636.84	3588	526.43	348.09	0.60	148.32	25.8	6.61	14298.84	68.61	6.66	2279.7	47.37	0.14	0.46	3.50	
Mt from exoskarn	M-1614-1	89.30	28404.06	4184	1501.78	537.08	0.03	146.94	27.8	25.99	15104.76	62.40	9.79	2501.1	51.63	0.07	0.12	5.17	
Mt from exoskarn	M-1614-1	89.96	23168.62	4746	2136.27	0.06	158.51	27.5	17.35	15230.45	54.66	11.10	2591.7	47.43	0.83	1.75	2.31	4.9	
Mt from exoskarn	M-1614-2	90.08	24550.80	4538	448.22	62.03	0.11	187.02	28.8	42.23	15468.38	63.60	8.60	2568.6	45.10	0.08	0.35	2.97	7.4
Mt from exoskarn	M-1614-2	90.10	23974.71	3904	1507.73	584.33	0.23	170.98	29.0	25.34	14795.76	63.98	8.02	2418.8	44.56	0.98	0.50	3.66	8.0
Mt from exoskarn	M-1614-2	90.47	20797.55	3858	2772.21	169.51	0.05	172.17	27.9	17.57	15153.50	64.40	8.53	2311.2	39.76	0.44	2.07	7.5	
Mt from exoskarn	M-1614-2	90.79	19362.22	3790	2033.34	51.20	0.04	163.23	25.9	7.34	14857.53	58.67	4.47	2797.5	41.15	0.64	1.78	2.39	
Mt from exoskarn	M-1614-2	90.35	22062.95	3611	2370.38	753.94	0.06	163.79	25.9	6.02	14408.69	59.66	8.51	2186.6	38.96	0.08	0.17	2.71	7.0
Mt from exoskarn	M-1614-2	91.01	22005.44	3300	400.43	81.25	0.04	166.37	25.4	7.69	13919.61	54.83	7.38	1923.8	41.04	0.61	0.20	2.83	7.4
Mt from exoskarn	M-1614-2	90.80	23169.17	3745	111.16	23.49	0.11	153.68	25.0	30.94	13784.41	54.44	6.88	2141.4	40.07	0.00	1.78	7.9	
Mt from exoskarn	M-1614-2	91.53	18853.81	3419	9844.69	63.80	0.09	149.42	22.3	16.74	12859.38	60.60	7.09	1789.1	37.73	0.25	1.99	8.5	
Mt from endoskarn	M-1025	95.25	197.30	2794	763.11	40.19	0.29	4277.53	434.0	10.17	5050.02	70.76	11.12	1455.9	31.24	1.69	1.14	1.76	
Mt from endoskarn	M-1025	95.13	318.30	3476	876.67	0.55	4195.62	432.7	16.56	5073.22	68.49	12.68	1653.1	32.94	1.57	1.41	1.81	5.4	
Mt from endoskarn	M-1025	95.41	184.32	2565	440.20	7.42	0.27	4101.04	431.7	15.63	4772.50	71.83	9.16	1366.1	31.38	0.99	1.12	1.36	7.8
Mt from endoskarn	M-1025	95.04	328.99	3728	707.95	30.45	0.07	4224.13	493.8	1.49	5967.90	64.98	11.00	1408.8	31.78	0.81	1.29	1.19	5.9
Mt from endoskarn	M-1025	94.89	405.44	3813	831.23	98.22	0.17	4543.68	480.6	0.36	5967.68	68.14	8.23	1687.6	33.50	1.31	1.25	1.70	8.3
Mt from endoskarn	M-1025	94.89	2340	407.53	37.50	0.44	4027.53	488.8	39.37	4602.73	488.8	39.37	69.82	11.46	1753.8	34.00	1.35	1.58	2.19
Mt from endoskarn	M-1025	94.97	280.69	1671	966.88	0.25	4642.33	531.6	3.51	5503.55	89.74	12.34	1744.5	36.44	1.76	1.77	0.10	7.3	
Mt from endoskarn	M-1025	94.94	274.52	1753	681.92	0.01	4592.04	563.4	4.17	6185.84	84.64	10.14	1707.3	38.05	1.02	1.42	0.34	8.4	
Mt from endoskarn	M-1002	95.20	526.09	1697	553.25	23.67	1.17	4921.44	313.7	9.07	4654.27	74.57	7.51	1022.8	25.00	1.71	0.71	3.31	9.9
Mt from endoskarn	M-1002	95.31	492.37	1763	528.51	33.85	0.88	3914.28	282.9	7.41	5106.39	71.50	8.21	1033.5	22.67	0.81	2.76	8.7	
Mt from endoskarn	M-1002	95.19	577.63	1704	380.85	13.07	1.35	4450.57	303.2	4.45	5768.00	76.51	6.98	864.1	22.66	1.37	0.43	2.51	11.0
Mt from endoskarn	M-1002	95.79	165.12	1353	293.69	33.68	0.67	4281.99	262.2	4.60	2234.49	51.51	6.09	1060.8	20.28	1.49	0.35	2.72	8.5
Mt from quartz diorite porphyry	M-910	93.79	1606.85	1712	923.83	0.92	8.10	8606.96	2331.0	117.35	4658.50	84.90	19.97	2535.5	65.71	2.02	2.10	10.74	4.3
Mt from quartz diorite porphyry	M-910	94.83	1382.80	1900	323.92	5.52	4121.40	2425.7	102.21	2920.78	85.77	24.52	2677.3	67.59	2.02	6.23	3.5		
Mt from quartz diorite porphyry	M-910	95.27	1128.14	1397	772.62	0.69	2095.09	2312.9	134.56	2903.49	103.80	35.62	2179.6	62.23	0.67	1.06	3.12	2.9	
Mt from quartz diorite porphyry	M-910	95.57	638.92	1091	553.22	222.30	0.35	2038.23	2273.5	105.43	2411.77	87.69	32.92	1669.6	56.84	0.90	1.13	3.94	2.7
Mt from quartz diorite porphyry	M-910	95.47	956.49	1308	608.35	1.91	1771.96	2918.5	315.74	1787.80	79.84	35.03	1775.8	59.47	0.86	0.83	2.3		
Mt from quartz diorite porphyry	M-910	95.70	689.49	610	239.76	17.28	1.09	2134.86	2714.2	150.19	2127.15	96.67	34.77	1509.2	57.64	1.36	0.96	0.22	2.8
Mt from quartz diorite porphyry	M-1537	95.56	295.45	1424	417.42	0.70	4253.23	1754.7	67.94	1447.69	78.83	29.47	1091.2	45.92	0.63	1.08	0.12	2.7	
Mt from quartz diorite porphyry	M-1537	95.63	322.89	2259	444.50	9.82	0.86	3054.11	1916.7	82.32	771.69	77.19	26.81	1169.6	49.56	0.76	1.88	2.96	2.9
Mt from quartz diorite porphyry	M-1537	95.73	319.96	937	378.41	19.67	0.57	3580.15	1734.3	88.77	1955.17	74.46	29.64	766.0	44.58	0.74	2.13	3.24	2.5
Mt from quartz diorite porphyry	M-2	94.90	145.63	2392.01	969.34	24.59	8.56	3160.05	1732.7	103.84	748.05	63.20	28.91	734.1	37.93	0.84	1.38	2.84	2.2
Mt from quartz diorite porphyry	M-2	95.30	70.25	2146.49	1088.86	16.74	3.75	5011.84	2476.76	82.51	621.01	17.42	27.61	64.66	42.17	1.49	2.20	4.76	0.6
Mt from quartz diorite porphyry	M-2	94.83	39.07	2161.70	2037.58	1115.25	3.68	5720.42	2351.77	79.89	919.51	16.18	22.91	83.60	36.21	1.21	2.22	4.23	0.7

(continued on next page)

Table A1 (continued)

Type	Sample	FeO/wt%	Mg/ppm	Al/ppm	Si/ppm	Ca/ppm	Sc/ppm	Ti/ppm	V/ppm	Cr/ppm	Mn/ppm	Co/ppm	Ni/ppm	Zn/ppm	Ga/ppm	Ge/ppm	Mo/ppm	Sn/ppm	Co/Ni
Mt from quartz diorite porphyry	M-2	94.19	301.32	3602.23	1979.98	162.78	2.10	8539.02	2026.01	82.68	1139.69	20.63	31.69	385.19	50.52	1.37	1.92	4.32	0.7
Mt from quartz diorite porphyry	M-2	93.67	197.06	2139.91	1463.87	6555.57	1.34	6865.60	1957.38	84.74	463.86	26.60	27.70	231.78	39.07	1.31	2.34	5.04	1.0
Mt from quartz diorite porphyry	M-1760	94.49	994.31	4037.32	1108.33	35.29	1.31	4747.17	1853.84	138.78	2693.22	103.18	35.51	1491.77	68.19	1.68	1.28	1.60	2.9
Mt from quartz diorite porphyry	M-1760	94.32	1414.58	4092.01	905.21	17.43	1.35	5241.99	1817.96	126.69	3226.15	106.91	36.47	1378.80	73.03	1.51	1.72	1.88	2.9
Mt from sodic-calcic alteration	M-1561-1	95.38	428.93	5864			1.53	3562.81	1441.3	24.83	1708.65	81.08	34.29	1967.5	62.85	2.78	0.85	3.79	2.4
Mt from sodic-calcic alteration	M-1561-1	95.75	223.96	3362	699.41	16.58	0.73	3140.65	1456.8	32.94	1468.95	89.16	35.31	644.7	57.78	2.75	0.99	2.15	2.5
Mt from sodic-calcic alteration	M-1561-1	95.64	304.45	4103	900.27	27.00	0.94	3145.22	1436.9	37.00	1324.35	91.15	36.87	690.7	57.96	2.07	0.82	2.12	2.5
Mt from sodic-calcic alteration	M-1561-1	94.81	755.44	5992	769.50		1.60	5939.29	1443.3	24.69	1430.79	94.39	33.18	1892.6	71.47	3.32	1.06	5.78	2.8
Mt from sodic-calcic alteration	M-1561-2	94.72	854.84	6679	489.38	10.28	1.71	5473.62	1479.9	21.20	2482.72	93.07	37.55	1908.6	66.22	2.06	1.42	5.77	2.5
Mt from sodic-calcic alteration	M-1561-2	94.52	484.02	5339	716.34	62.07	0.94	7425.13	1369.7	35.68	3152.85	86.10	36.01	1481.7	56.75	1.17	2.15	4.59	2.4
Mt from sodic-calcic alteration	M-1561-2	94.98	681.41	5997	607.12	34.25	1.11	4978.33	1449.2	28.63	1887.92	91.42	37.87	1619.9	62.54	1.44	1.54	3.75	2.4
Mt from sodic-calcic alteration	M-1561-2	95.32	548.49	4884	558.29	10.22	1.22	4403.20	1466.4	29.96	1291.32	88.24	35.59	1299.9	63.33	1.74	1.19	3.96	2.5
Mt from sodic-calcic alteration	M-1561-2	95.33	353.08	5246	596.08	2.64	0.96	4346.21	1457.3	31.61	1018.33	79.82	35.20	1568.3	61.09	1.94	1.17	3.48	2.3
Mt from sodic-calcic alteration	M-1561-2	95.37	385.71	5702	725.23	13.04	0.96	3508.26	1424.2	26.20	1373.81	76.02	34.80	1403.9	55.89	2.64	2.05	3.47	2.2
Mt from potassic alteration	M-1722	95.79	418.13	5015	761.66	190.91	0.90	1863.09	805.4	0.92	1646.79	102.44	29.30	962.1	52.61	1.43	2.38	2.54	3.5
Mt from potassic alteration	M-1722	95.84	148.97	4672	423.76	12.22	0.96	2279.29	851.0	3.65	1668.76	107.66	30.47	1310.9	42.48	1.38	1.90	2.68	3.5
Mt from potassic alteration	M-1722	95.16	784.61	5257	1774.44	302.84	1.28	2865.27	918.2	7.57	2281.06	104.73	31.56	1431.3	60.60	1.96	1.80	3.78	3.3
Mt from potassic alteration	M-1722	95.75	260.88	4244	863.49	93.58	1.30	2129.11	1168.2	45.28	1922.31	108.36	29.16	849.5	52.60	2.39	0.74	1.30	3.7
Mt from potassic alteration	M-1722	96.01	48.76	2889	610.31	103.77	1.17	2251.68	1214.7	36.90	1230.12	101.75	32.42	927.3	49.86	1.61	0.70	1.31	3.1
Mt from potassic alteration	M-10	95.30	248.46	1483	561.77	133.50	1.55	3384.17	1573.5	32.96	1128.00	118.95	43.39	1455.6	64.79	2.45	1.28	0.94	2.7
Mt from potassic alteration	M-10	95.60	132.86	2256	800.76	137.31	1.72	2776.70	1487.2	124.15	839.14	111.87	49.21	1711.5	59.32	1.75	2.35	2.45	2.3
Mt from potassic alteration	M-10	95.76	76.87	1676	1135.68	259.31	1.20	2320.78	1594.7	35.84	795.32	109.11	59.37	1222.4	60.92	1.83	1.81	1.44	1.8
Mt from potassic alteration	M-10	95.31	326.77	2579	562.32		1.49	3560.95	1516.7	37.71	1712.75	123.80	53.37	1987.9	67.04	3.35	2.21	0.80	2.3
Mt from potassic alteration	M-1695	95.67	121.31	4295	495.81	31.96	1.00	2501.59	1475.4	10.19	1626.72	103.33	32.06	1743.8	51.68	1.70	1.26	2.98	3.2
Mt from potassic alteration	M-1695	95.46	151.42	4733	495.26	9.65	1.31	3332.58	1509.3	12.19	1609.10	103.35	26.63	1940.9	51.05	2.05	1.38	3.67	3.9
Mt from potassic alteration	M-1695	95.57	206.82	5179	572.95	12.76	1.61	2220.70	1502.1	8.95	1660.47	117.09	29.82	1887.6	58.91	1.78	1.39	2.95	3.9
Mt from potassic alteration	M-854	92.78	2392.02	4298.42	4416.40	86.82	2.10	11467.57	1631.36	62.80	511.66	36.04	34.58	1375.42	44.57	1.84	2.29	2.69	1.0
M-854	94.43	756.84	1917.41	1446.10	18.59	1.45	9291.29	1704.72	15.76	749.97	42.41	33.22	1336.35	46.72	1.08	3.64	1.93	1.3	

(continued on next page)

Table A1 (continued)

Type	Sample	FeO/wt%	Mg/ppm	Al/ppm	Si/ppm	Ca/ppm	Sc/ppm	Ti/ppm	V/ppm	Cr/ppm	Mn/ppm	Co/ppm	Ni/ppm	Zn/ppm	Ga/ppm	Ge/ppm	Mo/ppm	Sn/ppm	Ge/Ni
Mt from potassic alteration	M-854	92.54	2278.84	4602.10	5157.59	56.41	2.27	11702.33	1660.89	23.33	633.27	36.91	31.95	1336.51	48.47	1.65	1.96	2.65	1.2
Mt from potassic alteration	M-854	93.57	1360.11	2531.78	2484.66	43.88	2.16	12027.18	1737.52	72.15	553.33	37.02	26.66	1319.08	54.82	1.90	3.74	2.52	1.4
Mt from potassic alteration	M-854	94.02	965.43	2618.94	2512.07	37.19	2.04	9323.01	1851.20	18.62	742.27	38.74	28.56	1300.46	57.20	1.88	3.76	2.16	1.4
Mt from potassic alteration	M-854	94.59	763.95	2389.90	1313.69	1.69	7876.79	1590.76	27.90	855.51	52.16	42.54	1498.12	48.74	1.91	3.79	3.02	1.2	
Mt from potassic alteration	M-854	92.76	2487.64	4205.56	3861.62	192.55	2.23	11765.22	1605.87	29.86	764.15	48.83	44.97	1747.75	53.15	1.81	5.30	4.29	1.1
Mt from potassic alteration	M-854	93.92	1839.19	2630.73	1764.92	205.17	1.69	8636.34	1672.92	9.77	2403.25	71.31	40.57	1477.29	48.25	1.83	4.60	3.94	1.8
Mt from potassic alteration	M-854	94.53	1659.96	2499.47	1051.66	1.25	6551.29	1641.40	26.94	2107.46	62.91	40.44	1477.08	54.46	1.49	3.66	3.97	1.6	
Mt from potassic alteration	M-854	93.02	2978.49	2848.83	2510.39	221.20	2.77	12422.21	1675.52	54.99	1598.24	65.06	43.68	1437.87	53.20	1.70	6.59	4.81	1.5
Mt from potassic alteration	M-854	94.45	1322.70	2604.94	1715.14	73.20	1.57	6852.28	1582.28	6.23	1359.43	54.30	44.89	1630.06	53.29	2.24	6.26	4.74	1.2
Mt from potassic alteration	M-1110	94.85	40.11	984.29	1735.04	456.21	1.85	7882.80	2207.02	96.66	987.86	26.58	28.73	160.29	50.81	1.53	0.61	2.20	0.9
Mt from potassic alteration	M-1110	91.02	310.41	3080.01	6553.27	5393.87	2.36	18152.60	2090.44	64.90	1334.11	20.51	24.06	345.61	60.28	2.11	4.49	3.69	0.9
Mt from potassic alteration	M-1110	93.75	2357.55	3891.78	3592.10	123.35	0.64	6538.20	2009.63	85.68	1441.74	21.21	20.47	545.67	51.31	1.42	3.13	1.96	1.0
Mt from potassic alteration	M-1110	95.13	774.65	1608.67	2984.51	204.56	0.21	4645.42	1126.16	3.32	696.08	38.11	41.66	293.86	32.00	1.75	0.64	1.39	0.9
Mt from potassic alteration	M-1110	93.65	97.77	1936.46	2709.90	795.97	0.40	11770.87	1152.69	1.18	3280.95	24.20	42.32	460.30	36.09	2.47	3.48	2.42	0.6
Standard reference material	GSE-1G	12.697755	21.000	68.800	251.000	53.000	530	450	440	400	590	380	440	460	490	320	390	280	
Average content	GSE-1G	14.130093	22.081	72.523	270.221	52.947	554	474	461	421	619	400	462	487	517	341	411	304	
Standard reference material	GSD-1G	12.99365	21.600	72.500	248.800	50.600	49.6	8100	45	49	205	38.8	59	48	52	34	34	29	
Average content	GSD-1G	13.90521	23.092	77.714	269.798	52.975	50	8513	44	45	230	45	66	60	42	41	36	36	
Standard reference material	BCR-2G	12.399956	21470.36	70912.8	254.320	50457.82	33	14.100	425	17	1550	38	13	125	23	1.5	270	2.6	
Average content	BCR-2G	13.0587669	22467.88	74110.1	274.835	50550.40	30	14.649	440	16	1615	41	13	160	24	2	272	3.2	
Standard reference material	NIST 610	0.0589217	465	10795.68	327.250	82190.5	441	434	442	405	485	405	458.7	456	438	426	410	396	
Average content	NIST 610	0.0720957	581	12756.07	376.270	101802.9	534	603	520	496	523	477	545.9	512	518	503	486	467	

Appendix B

See Table A2.

Table A2
Major element concentrations in hydrothermal biotites analyzed by EMPA.

Type	Hydrothermal						
Sample	1C3-1	1C3-2	1C3-3	1C4-1	1C4-2	1756C1-1	1756C4-1
SiO ₂	41.06	38.71	38.92	37.69	38.20	37.69	36.53
Al ₂ O ₃	12.06	12.32	13.34	12.38	11.81	12.85	13.68
TiO ₂	3.25	3.15	3.25	4.00	3.82	3.98	2.73
FeO*	12.44	12.56	13.64	13.73	13.75	13.71	14.42
MnO	0.18	0.25	0.34	0.25	0.27	0.21	0.28
MgO	17.57	18.69	18.35	16.48	17.13	17.11	19.90
CaO	0.11	0.19	0.03	0.04	0.06	0.07	0.15
Na ₂ O	0.28	0.16	0.16	0.28	0.32	0.18	0.10
K ₂ O	9.75	9.01	8.02	10.14	10.11	9.94	6.09
F	0.11	0.37	0.24	0.13	0.04	0.11	0.15
Cl	0.20	0.20	0.22	0.21	0.26	0.20	0.14
Total	95.40	96.66	95.25	95.71	96.00	95.07	
Based on O = 22							
Si	5.932	5.616	5.530	5.583	5.626	5.502	5.361
Al	2.054	2.106	2.235	2.161	2.050	2.210	2.288
Ti	0.353	0.344	0.348	0.445	0.423	0.437	0.292
Fe ³⁺	0.204	0.901	1.130	0.653	0.682	0.848	1.671
Fe ²⁺	1.298	0.623	0.490	1.048	1.010	0.826	0.020
Mn	0.022	0.031	0.041	0.031	0.033	0.025	0.034
Mg	3.785	4.042	3.888	3.640	3.760	3.723	4.212
Na	0.078	0.046	0.043	0.080	0.090	0.050	0.028
K	1.797	1.667	1.454	1.916	1.899	1.851	1.102
Ca	0.030	0.017	0.030	0.004	0.007	0.009	0.023
F	0.030	0.101	0.064	0.037	0.012	0.030	0.040
Cl	0.040	0.040	0.040	0.045	0.044	0.053	0.027
OH	3.930	3.859	3.897	3.918	3.944	3.916	3.933
Fe ³⁺ /Fe ²⁺	0.157	1.445	2.305	0.624	0.675	1.027	-5.034
XMg	0.668	0.680	0.659	0.626	0.636	0.635	0.674
XsId	0.021	0.061	0.102	0.089	0.053	0.106	0.137
Xan	0.310	0.259	0.238	0.285	0.311	0.258	0.189
XF/XCl	0.746	2.547	1.604	0.828	0.279	0.567	1.453
XCl/XOH	0.010	0.010	0.010	0.011	0.011	0.014	0.007
XF/XOH	0.008	0.026	0.016	0.009	0.003	0.008	0.010
IV(F)	3.270	2.736	2.909	3.114	3.617	3.207	3.015
IV(Cl)	-4.308	-4.291	-4.274	-4.284	-4.372	-4.313	-4.150
IV(F/Cl)	7.578	7.072	7.200	7.388	7.901	7.578	7.328
Type	Hydrothermal						
Sample	1756C4-2	910C3-1	910C3-2	910C1-1	910C1-2	868C5-1	868C5-2
SiO ₂	36.31	38.55	38.75	39.22	39.04	38.32	38.98
Al ₂ O ₃	13.48	12.05	12.13	12.07	12.14	12.58	12.65
TiO ₂	3.13	4.01	4.14	3.42	3.40	3.72	2.23
FeO*	15.32	13.22	13.39	13.41	13.67	13.74	13.58
MnO	0.23	0.28	0.26	0.33	0.30	0.26	0.32
MgO	18.96	17.20	16.89	17.95	17.72	17.15	18.33
							17.37

Table A2 (continued)

Type	Hydrothermal						
CaO	0.16	0.04	0.02	0.002	0.02	0.03	0.25
Na2O	0.10	0.21	0.27	0.14	0.29	0.17	0.25
K2O	5.23	9.72	9.67	9.62	9.13	9.45	9.62
F	0.02	0.31	0.15	0.09	0.07	0.07	0.11
Cl	0.14	0.22	0.17	0.15	0.14	0.22	0.29
Total	95.80	95.76	96.43	95.93	96.25	95.56	96.64
Based on O = 22							
Si	5.185	5.641	5.673	5.662	5.590	5.693	5.619
Al	2.268	2.079	2.088	2.057	2.075	2.163	2.145
Ti	0.336	0.441	0.455	0.372	0.371	0.408	0.411
Fe3+	2.297	0.741	0.688	0.770	0.809	0.721	0.757
Fe2+	-0.468	0.877	0.948	0.852	0.849	0.955	0.886
Mn	0.028	0.035	0.032	0.040	0.037	0.032	0.034
Mg	4.036	3.752	3.678	3.871	3.832	3.730	3.746
Na	0.028	0.058	0.077	0.059	0.082	0.065	0.070
K	0.953	1.814	1.803	1.775	1.690	1.849	1.776
Ca	0.024	0.005	0.003	0.003	0.005	0.005	0.005
F	0.006	0.085	0.043	0.024	0.024	0.018	0.030
Cl	0.027	0.044	0.035	0.030	0.029	0.044	0.058
OH	3.967	3.871	3.923	3.970	3.948	3.938	3.912
Fe3+/Fe2+	-4.909	0.845	0.726	0.903	0.953	0.755	0.855
XMg	0.648	0.642	0.634	0.656	0.650	0.638	0.642
Xsid	0.144	0.059	0.060	0.048	0.054	0.086	0.078
Xan	0.208	0.300	0.306	0.297	0.296	0.276	0.280
XF/XCl	0.208	1.927	1.221	0.831	0.414	0.521	0.414
XCl/XOH	0.007	0.011	0.009	0.008	0.007	0.011	0.015
XF/XOH	0.001	0.022	0.011	0.006	0.005	0.004	0.008
IV(F)	3.950	2.772	3.069	3.344	3.439	3.498	3.225
IV(Cl)	-4.094	-4.305	-4.182	-4.161	-4.123	-4.288	-4.353
IV(F/Cl)	8.044	7.077	7.251	7.467	7.727	7.851	7.642

Reference

- Ayati, F., Yavuz, F., Noghreyan, M., Haroni, H.A., Yavuz, R., 2008. Chemical characteristics and composition of hydrothermal biotite from the Dalli porphyry copper prospect, Arak, central province of Iran. *Miner. Petrol.* 94, 107–122.
- Afshoony, S.Z., Mirnejad, H., Esmaily, D., Haroni, A.H., 2013. Mineral chemistry of hydrothermal biotite from the Kahang porphyry copper deposit (NE Isfahan), Central Province of Iran. *Ore Geol. Rev.* 54, 214–232.
- Bajwah, Z.U., Seccombe, P.K., Offler, R., 1987. Trace element distribution Co: Ni ratios and genesis of the Big Cadia iron-copper deposit, New South Wales, Australia. *Miner. Depos.* 22, 292–300.
- Balan, E., De Villiers, J.P.R., Eeckhout, S.G., Glatzel, P., Toplis, M.J., Fritsch, E., Allard, T., Galois, L., Calas, G., 2006. The oxidation state of vanadium in titanomagnetite from layered basic intrusions. *Am. Mineral.* 91, 953–956.
- Bian, Y.C., 1995. On the Origin of Magushan Cu-Mo deposit in south Anhui. *Geol. Jiangsu* 19, 17–20 (in Chinese with English abstract).
- Boomeri, M., Nakashima, K., Lentz, D.R., 2009. The Miduk porphyry Cu deposit, Kerman, Iran: a geochemical analysis of the potassic zone including halogen element systematics related to Cu mineralization processes. *J. Geochem. Explor.* 103, 17–29.
- Buddington, A.F., Lindsley, D.H., 1964. Iron-titanium oxide minerals and synthetic equivalents. *J. Petrol.* 5, 310–357.
- Carten, R.B., 1986. Sodium-calcium metasomatism: Chemical, temporal and spatial relationships at the Yerington, Nevada, porphyry copper deposit. *Econ. Geol.* 81, 1495–1519.
- Chang, Y.F., Liu, X.P., Wu, Y.C., 1991. The Copper-Iron Belt of the Lower and Middle reaches of the Changjiang River. Geological Publishing House, Beijing 1–379 (in Chinese).
- Canil, D., Grondahl, C., Lacourse, T., Pisiak, L.K., 2016. Trace elements in magnetite from porphyry Cu-Mo-Au deposits in British Columbia, Canada. *Ore Geol. Rev.* 72, 1116–1128.
- Czamanske, G.K., Wones, D.R., 1973. Oxidation during magmatic differentiation, Finnmarka complex, Oslo Area, Norway: Part 2, the mafic silicates. *J. Petrol.* 14, 349–380.
- Dare, S.A.S., Barnes, S.J., Beaudoin, G., Méric, J., Boutroy, E., Potvin-Doucet, C., 2014. Trace elements in magnetite as petrogenetic indicators. *Miner. Depos.* 49, 785–796.
- Dymek, R.F., 1983. Titanium, aluminum and interlayer cation substitutions in biotite from high-grade gneisses, West Greenland. *Am. Mineral.* 68, 880–899.
- Dilles, J.H., Einaudi, M.T., 1992. Wall-rock alteration and hydrothermal flow paths about the Ann-Mason porphyry copper deposit, Nevada: a 6-km vertical reconstruction. *Econ. Geol.* 87, 1963–2001.
- Dilles, J.H., Proffett, J.M., 1995. Metallogenesis of the Yerington batholith, Nevada. *Arizona Geological Society Digest* 20, 306–315.
- Du, H.F., Lai, T.G., Jiang, Y.Y., Fan, P.F., Gong, W.Q., 2017. Mineral chemistry of biotites from the granodiorite porphyry around the Jinjiwo copper deposit in the Jirui ore district: implications for petrogenesis and mineralization. *Acta Petrologica Et Mineralogica* 36 (3), 329–342 (in Chinese with English abstract).
- Dupuis, C., Beaudoin, G., 2011. Discriminant diagrams for iron oxide trace element fingerprinting of mineral deposit types. *Miner. Deposita* 46, 319–335.
- Duan, C., Li, Y.H., Yuan, S.D., Hu, M.Y., Zhao, L.H., Chen, X.D., Zhang, C., Liu, J.L., 2012. Geochemical characteristics of magnetite from Washan iron deposit in Ningwu ore district and its constraints on ore-forming. *Acta Petrologica Sinica* 28, 243–257 (in Chinese with English abstract).
- Einaudi, M.T., 1982. General features and origin of skarns associated with porphyry copper plutons, advances in geology of the Porphyry Copper Deposits, Southwestern North America. The University of Arizona Press, Tucson, pp. 185–209.
- Foster, M.D., 1960. Interpretation of the composition of trioctahedral micas. *US Geol. Surv. Prof. Pap.* 354-B, 1–146.
- Frost, B.R., Lindsley, D.H., 1991. Occurrence of iron-titanium oxides in igneous rocks. *Petrologic and Magnetic Significance* 489–509.
- Gao, R.R., 2003. Composition of the continental crust. *Treatise Geochem.* 3, 1–64.
- Hong, D.J., Huang, Z.Z., Chan, S.W., Wang, X.H., 2017. Geological characteristics and exploration directions of the Cu-polymetallic ore deposits in the Magushan-Qiaomaishan areas in Xuancheng, Anhui Province. *East China Geol.* 38, 28–36 (in Chinese with English abstract).
- Hu, H., Duan, Z., Luo, Y., Li, J.W., 2014. Trace element systematics of magnetite from the Chengchao iron deposit in the Daye district: a laser ablation ICP-MS study and insights into ore genesis. *Acta Petrologica Sinica* 30, 1292–1306 (in Chinese with English abstract).
- Huang, J.M., Yi, H., Chen, B.X., 2013. Geological characteristics of Kunshan Cu-poly-metallic mineralization district in Xuancheng City, Anhui Province. *J. Hefei Univ. Technol.* 36, 217–223 (in Chinese with English abstract).
- Ilton, E.S., Eugster, H.P., 1989. Base metal exchange between magnetite and a chloride rich hydrothermal fluid. *Geochim. Cosmochim. Acta* 53, 291–301.
- Jacobs, D.C., Parry, W.T., 1976. A comparison of the geochemistry of biotite from some basin and range stocks. *Econ. Geol.* 71, 1029–1035.
- Jacobs, D.C., Parry, W.T., 1979. Geochemistry of biotite in the Santa Rita porphyry copper deposit, New Mexico. *Econ. Geol.* 74, 860–887.
- Jiang, F., 2017. Characteristics and Genesis of Magmatic Rocks in the Chating Cu-Au Ore District, Xuancheng City. Hefei University of Technology (D), Anhui Province.
- Jiang, G.H., 2004. Chlorine and fluorine control on copper and tungsten mineralization in hydrothermal deposits-Cases of Dexing porphyry copper deposit and Dajishan tungsten deposit in Jiangxi Province [D]. Institute of Geochemistry, Chinese Academy of Sciences (in Chinese with English abstract).
- Jin, C., Gao, X.Y., Chen, W.T., Zhao, T.P., 2018. Magmatic-hydrothermal evolution of the Donggou porphyry Mo deposit at the southern margin of the North China Craton: evidence from chemistry of biotite. *Ore Geol. Rev.* 92, 84–96.
- Jurek, K., Hulinský, V., 1980. The use and accuracy of the ZAF correction procedure for the microanalysis of glasses. *Microchim. Acta* 73, 183–198.
- John, D.A., 1989. Evolution of hydrothermal fluids in the Park Premier stock, central Wasatch Mountains, Utah. *Econ. Geol.* 84, 879–902.
- Liu, Y.S., Hu, Z.C., Gao, S., Gunther, D., Xu, J., Gao, C.G., Chen, H.H., 2008. In situ analysis of major and trace elements of anhydrous minerals by LA-ICP-MS without applying an internal standard. *Chem. Geol.* 257, 34–43.
- Liu, B., Ma, C.Q., Liu, Y.Y., Xiong, F.H., 2010. Mineral chemistry of biotites from the Tongshankou Cu-Mo deposit: Implications for petrogenesis and mineralization. *Acta Petrologica Et Mineralogica* 29 (2), 151–165 (in Chinese with English abstract).
- Li, J.X., Li, G.M., Qin, K.Z., Xiao, B., Chen, L., Zhao, J.X., 2011. Mineralogy and Mineral Chemistry of the Cretaceous Duolung Gold-Rich Porphyry Copper Deposit in the Bangongco Arc, Northern Tibet. *Resour. Geol.* 62, 19–41.
- Li, W., Xie, G.Q., Zhu, Q.Q., Zheng, X.W., Zhang, Z.Y., Han, Y.X., 2016. Multi-superimposed mineralization process in Chengchao iron deposit, southern Hubei Province: Evidence from the study of magnetite. *Acta Petrologica Sinica* 32, 471–492 (in Chinese with English abstract).
- Lindsley, D.H., 1976. The crystal chemistry and structure of oxide minerals as exemplified by the Fe-Ti oxides. In: Rumble III (ed) *Oxide Minerals. Reviews in Mineralogy, Mineralogical Society of America*, pp. L1–L60.
- Loferer, P.J., Ayuso, R.A., 1995. Petrography and mineral chemistry of the composite Beboullie pluton, northern Maine, USA: Implications for the genesis of Cu-Mo mineralization. *Chem. Geol.* 123, 89–105.
- Mao, J.W., Xie, G.Q., Duan, C., Pirajno, F., Ishiyama, D., Chen, Y.C., 2011. A tectono-genetic model for porphyry-skarn-stratabound Cu-Au-Mo-Fe and magnetite-apatite deposits along the Middle-Lower Yangtze River Valley, Eastern China. *Ore Geol. Rev.* 43, 294–314.
- Meinert, L.D., 1987. Skarn zonation and fluid evolution in the Groundhog Mine, Central mining district, New Mexico. *Econ. Geol.* 82, 523–545.
- Mollo, S., Putirka, K., Izeki, G., Scarlato, P., 2013. The control of cooling rate on titanomagnetite composition: implications for a geospeedometry model applicable to alkaline rocks from Mt. Etna volcano. *Contrib. Mineral. Petrol.* 165, 457–475.
- Munoz, J.L., 1984. F-OH and Cl-OH exchange in micas with applications to hydrothermal ore deposits. *Rev. Mineral. Geochim.* 13, 469–493.
- Nachit, H., Razafimahafela, N., Stussi, J.M., Caron, J.P., 1985. Composition chimique des biotites et typologie magmatique des granitoïdes. *C.R. Acad. Sci. Paris Ser. II* 301, 813–818.
- Nachit, H., Ibib, A., Abia, E.H., Ohoud, M.B., 2005. Discrimination between primary magmatic biotites, reequilibrated biotites and neofomed biotites. *C. R. Geosci.* 337, 1415–1420.
- Nadol, P., Angerer, T., Mauk, J.L., French, D., Walshe, J., 2014a. The chemistry of hydrothermal magnetite: a review. *Ore Geol. Rev.* 61, 1–32.
- Nadol, P., Mauk, J.L., Leveille, R.A., Koenig, A.E., 2014b. Geochemistry of magnetite from porphyry Cu and skarn deposits in the southwestern United States. *Miner. Depos.* 1–23.
- Nadol, P., Mauk, J.L., Hayes, T.S., Koenig, A.E., Box, S.E., 2012. Geochemistry of magnetite from hydrothermal ore deposits and host rocks of the Mesoproterozoic Belt Supergroup, United States. *Econ. Geol.* 107, 1275–1292.
- Nadol, P., Koenig, A.E., 2011. LA-ICP-MS of magnetite: methods and reference materials. *J. Anal. At. Spectrom.* 26, 1872–1877.
- Nadol, P., Mauk, J.L., Leveille, R.A., Koenig, A.E., 2010. Geochemistry of magnetite from Cu-Mo porphyry + skarn, and Climax Mo deposits in the western United States. In: *Ima*. p. 507.
- Nadol, P., Mauk, J.L., Leveille, R.A., Koenig, A.E., 2015. Geochemistry of magnetite from porphyry Cu and skarn deposits in the southwestern United States. *Miner Deposita*. 50, 493–515.
- Nielsen, R.L., Forsythe, L.M., Gallahan, W.E., Fisk, M.R., 1994. Major- and trace-element magnetite-melt equilibria. *Chem. Geol.* 117, 167–191.
- Ning, S.Y., Wang, F.Y., Xue, W.D., Zhou, T.F., 2017. Geochemistry of the Baoshan pluton in the Tongling region of the lower Yangtze River Belt. *Geochimica* 46, 397–412 (in Chinese with English abstract).
- Pass, H.E., Cooke, D.R., Davidson, G., Maas, R., Dipple, G., Rees, C., Ferreira, L., Taylor, C., Deyell, C.L., 2014. Isotope geochemistry of the northeast zone, Mount Polley alkalic Cu-Au-Ag porphyry deposit, British Columbia: a case for carbonate assimilation. *Econ. Geol.* 109, 859–890.
- Parsapoor, A., Khalili, M., Tepley, F., Maghami, M., 2015. Mineral chemistry and isotopic composition of magmatic, re-equilibrated and hydrothermal biotites from Darreh-Zar porphyry copper deposit, Kerman (southeast of Iran). *Ore Geol. Rev.* 66, 200–218.
- Pirajno, F., Zhou, T.F., 2015. Intracontinental porphyry and porphyry skarn mineral systems in eastern China: scrutiny of a special case “made-in-China”. *Econ. Geol.* 110 (3), 603–629.
- Pisiak, L.K., Canil, D., Lacourse, T., Plouffe, A., Ferbey, T., 2017. Magnetite as an indicator mineral in the exploration of porphyry deposits: A case study in till near the Mount Polley Cu-Au Deposit, British Columbia, Canada. *Econ. Geol.* 112 (4), 919–940.
- Pokrovski, G.S., Dubrovinsky, L.S., 2011. The S^{2-} ion is stable in geological fluids at elevated temperatures and pressures. *Science* 331, 1052–1054.
- Qian, S.L., Yang, Q.G., Xie, Z.J., Liu, J., 2017. Geological features and a discussion of ore-forming conditions of the Chating porphyry copper (gold) ore deposit in the Xuanzhou district, Anhui Province. *Geol. Anhui* 27, 81–86 (in Chinese with English abstract).
- Ray, G.E., Webster, I.C.L., 2007. Geology and chemistry of the low Ti magnetite-bearing Heff Cu-Au skarn and its associated plutonic rocks, Heffley Lake, South-Central British Columbia. *Explor. Min. Geol.* 16, 159–186.
- Righter, K., Leeman, W.P., Hervig, R.L., 2006a. Partitioning of Ni, Co and V between

- spinel structured oxides and silicate melts: importance of spinel composition. *Chem. Geol.* 227, 1–25.
- Righter, K., Sutton, S.R., Newville, M., Le, L., Schwandt, C.S., Uchida, H., et al., 2006b. An experimental study of the oxidation state of vanadium in spinel and basaltic melt with implications for the origin of planetary basalt. *Am. Mineral.* 91, 1643–1656.
- Robert, J.L., 1976. Titanium solubility in synthetic phlogopite solid solutions. *Chem. Geol.* 17, 213–227.
- Sillitoe, R.H., 2010. Porphyry copper systems. *Econ. Geol.* 105, 3–41.
- Seedorff, E., Dilles, J.H., Proffett, J.M., Einaudi, M.T., 2005. Porphyry deposits: Characteristics and Origin of Hypogene Features. *Econ. Geol., Economic Geology 100th Anniversary Volume*, 251–298.
- Seedorff, E., Barton, M.D., Stavast, W.J.A., Maher, D.J., 2008. Root zones of porphyry systems: extending the porphyry model to depth: *Econ. Geol.* 103, 939–956.
- Selby, D., Nesbitt, B.E., 2000. Chemical composition of biotite from the Casino porphyry Cu-Au-Mo mineralization, Yukon, Canada: evaluation of magmatic and hydrothermal fluids chemistry. *Chem. Geol.* 171, 77–93.
- Speer, J.A., 1987. Evolution of magmatic AFM mineral assemblages in granitoid rocks: the hornblende + melt = biotite reaction in the Liberty Hill pluton, South Carolina. *Am. Mineral.* 72, 863–878.
- Sun, W.D., Liang, H.Y., Ling, M.X., Zhan, M.Z., Ding, X., Zhang, H., Yang, X.Y., Li, Y.L., Ireland, T.R., Wei, Q.R., Fan, W.M., 2003. The link between reduced porphyry copper deposits and oxidized magmas. *Geochim. Cosmochim. Acta* 103, 263–275.
- Tang, P., Chen, Y.C., Tang, J.X., Zheng, W.B., Leng, Q.F., Lin, B., Fang, X., 2016. Characteristics and geological significance of biotites in Jiamal porphyry deposit system, Tibet. *Mineral Deposits* 35, 846–866 (in Chinese with English abstract).
- Tang, P., Tang, J.X., Zheng, W.B., Leng, Q.F., Lin, B., Tang, X.Q., 2017. Mineral chemistry of hydrothermal biotites from Lakang'e porphyry Cu-Mo deposit, Tibet. *Earth Sci. Front.* 24, 265–282 (in Chinese with English abstract).
- Taylor, R.P., 1983. Comparison of biotite geochemistry of Bakircay, Turkey and Los Pelambres, Chile, porphyry copper systems. *Institution of Mining and Metallurgy Transactions* 92, 16–22.
- Toplis, M.J., Carroll, M.R., 1995. An experimental study of the influence of oxygen fugacity on Fe-Ti oxide stability, phase relations, and mineral–melt equilibria in ferro-basaltic systems. *J. Petrol.* 36, 1137–1170.
- Toplis, M., Corgne, A., 2002. An experimental study of element partitioning between magnetite, clinopyroxene and iron-bearing silicate liquids with particular emphasis on vanadium. *Contrib. Mineral. Petrol.* 144, 22–37.
- Uchida, E., Endo, S., Makino, M., 2007. Relationship between solidification depth of granitic rocks and formation of hydrothermal ore deposits. *Resour. Geol.* 57, 47–56.
- Wang, F.Y., Ge, C., Ning, S.Y., Nie, L.Q., Zhong, G.X., White, N.C., 2017. A new approach to LA-ICP-MS mapping and application in geology. *Acta Petrologica Sinica* 33, 3422–3436 (in Chinese with English abstract).
- Wang, S.W., Zhou, T.F., Yuan, F., Fan, Y., Cao, X.S., Wang, B., 2012. Re-Os and $^{40}\text{Ar}/^{39}\text{Ar}$ dating of the Shuijadian copper deposit in Tongling, China: Implications for regional metallogenesis. *Acta Petrologica Sinica* 28, 3170–3180 (in Chinese with English abstract).
- Wang, S.W., Zhou, T.F., Yuan, F., Fan, Y., Yu, C.H., Ge, L.H., Shi, C., Chi, Y.Y., 2014. Emplacement sequences and geochronology of the Shaxi porphyry copper-gold deposit, Anhui Province, East China. *Acta Petrologica Sinica* 30, 979–994 (in Chinese with English abstract).
- Wang, S.W., 2015. Porphyry deposits and associated magmatic activity in the Anhui segment of the Middle-Lower Yangtze River Valley metallogenic belt. PhD thesis, Hefei University of Technology (in Chinese with English abstract).
- Wechsler, B.A., Lindsley, D.H., Prewitt, C.T., 1984. Crystal structure and cation distribution in titanomagnetites ($\text{Fe}_3\text{xTi}x\text{O}_4$). *Am. Mineral.* 69, 754–770.
- Wones, D.R., Eugster, H.P., 1965. Stability of biotite: experiment, theory, and application. *Am. Mineral.* 50, 1228–1272.
- Wood, B.J., Nell, J., Woodland, A.B., 1991. Macroscopic and microscopic thermodynamic properties of oxides. *Oxide Minerals: Petrologic and Magnetic Significance, Volume 25: Reviews in Mineralogy*, Mineralogical Society of America, pp. 265–302.
- Xiao, Q.L., Zhou, T.F., Yuan, F., Wang, S.W., Xie, Z.J., Liu, J., 2018. Compositional characteristics, petrogenesis and metallogenic significance of biotite from the ore-bearing quartz diorite porphyry in the Chating Cu-Au deposit, Xuancheng, Anhui province. *Mineral Deposits* (submitted) (in Chinese with English abstract).
- Zhang, W., 2015. Ore genesis of the Jiguanzui Cu-Au deposit in Southeastern Hubei Province, China. PhD thesis, China University of Geoscience (in Chinese with English abstract).
- Zhou, T.F., Fan, Y., Yuan, F., Zhong, G.X., 2012. Progress of geological study in the Middle-Lower Yangtze River Valley metallogenic belt. *Acta Petrologica Sinica* 28, 3051–3066 (in Chinese with English abstract).
- Zhou, T.F., Wang, S.W., Fan, Y., Yuan, F., Zhang, D.Y., White, N.C., 2015. A review of the intracontinental porphyry deposits in the Middle-Lower Yangtze River Valley metallogenic belt, Eastern China. *Ore Geol. Rev.* 65, 433–456.
- Zhou, T.F., Wang, S.W., Yuan, F., Fan, Y., Zhang, D.Y., Chang, Y.F., White, N.C., 2016. Magmatism and related mineralization of the intracontinental porphyry deposits in the Middle-Lower Yangtze River Valley Metallogenic Belt. *Acta Petrologica Sinica* 32, 271–288 (in Chinese with English abstract).
- Zhou, T.F., Fan, Y., Wang, S.W., White, N.C., 2017. Metallogenic regularity and metallogenic model of the Middle-Lower Yangtze River Valley Metallogenic Belt. *Acta Petrologica Sinica* 33, 3353–3372 (in Chinese with English abstract).